Vibration Analysis and Control in Hard-Disk Drive Servo Systems

Pang Chee Khiang

NATIONAL UNIVERSITY OF SINGAPORE

2003

Vibration Analysis and Control in Hard-Disk Drive Servo Systems

Pang Chee Khiang

B.Eng.(Hons), NUS

A DISSERTATION SUBMITTED

FOR THE DEGREE OF MASTER OF ENGINEERING

DEPARTMENT OF ELECTRICAL AND COMPUTER ENGINEERING

NATIONAL UNIVERSITY OF SINGAPORE

2003

Acknowledgments

My sincere thanks go to Dr Guo Guoxiao, my supervisor and teacher, for his motivation and patience with me all these years since my Industrial Attachment at the Institute in January 2000. He is my role model and has given me sound advice on my control theory and offered me his valuable opinions and visions pertaining to hard-disk drives.

Special thanks also has to go to Dr Ong Eng Hong, the assistant manager of Mechatronics and Micro Systems Group. His advice and patience on mechanical aspects of hard-disk drives were definitely very useful. I have to thank Dr Wu Daowei, my fellow student in the institute as well for being so patient and helpful despite his own busy schedule in finishing his Ph.D. thesis.

I am grateful to Ms Wong Wai Ee, my fellow student for her help and companionship in the laboratory. I also have to thank the staff of Mechatronics and Micro Systems Group who had helped me in one way or another.

I have to thank my sisters Ms Pang Chia-Li and Ms Pang Chia Mei for listening to my grievances and tolerate my frustration during times of setback. Not to forget my fiancée Ms Yong Leong Chu, my buddy Mr Tan Yeong Jong, and my pet Jack Russell Milo for whom so much of their time I've robbed.

Last but not least, I would like to thank Data Storage Institute for giving me financial support in the form of a Research Scholarship.

Contents

Summary

Track densities in magnetic recording demonstration are projected to exceed 200,000 Tracks-Per-Inch (TPI) in the year 2003 and it is still increasing. At the same time, the rotation speed of the disk-spindle assembly is also rapidly increasing to reduce rotational latency. However, the disk platters vibrate at their natural frequencies due to air flow and other excitation sources such as eccentricities of the disk-spindle assembly. This phenomenon contributes to TMR (Track Mis-Registration) and limits achievable TPI. As storage densities in Hard Disk Drives (HDDs) continue to increase, vibrations and other mechanical disturbances causing slider/head off-track have to be suppressed for better servo positioning. This dissertation studies and analyzes the disk fluttering phenomenon with its effect on the head positioning mechatronics and proposes some control technologies for suppressing high frequency vibrations.

After a brief introduction of HDD servo technology and some fundamentals of HDD servo control, the natural modes of an annul disk used in current HDDs are characterized and verified using Finite Element Modelling (FEM) analysis and Scanning Laser Doppler Vibrometer (SLDV) measurements. On decoupling the repeated and non-repeatable axial vibrations, a Recursive Least Squares (RLS) algorithm is implemented to identify natural frequencies and vibration amplitudes of forward and backward travelling waves of balanced and imbalanced disks based on rotation speed. With these data, the actual head off-track displacement is projected as a function of rotation speed. A disk fluttering vibration model is built for future simulations and designs of servo controller using the identified results.

A high track density exerts very stringent requirements on the HDD servo positioning system. As such, the disturbance rejection capability should be strengthened not only by increasing the gain crossover frequency but also reshaping the sensitivity frequency response. In a single stage servo system using VCM as the sole actuator, the sensitivity hump is unavoidable from Bode's Integral Theorem (BIT), which would cause higher frequency disturbances to be amplified. Dual-stage actuation is capable of better disturbance rejection via high bandwidth servos. The fundamentals of HDD dual-stage control system are introduced, including actuator modelling, control structures and design methodology. By modelling the secondary actuator as a pure gain for many frequencies, the sensitivity limitation in a Decoupled Master-Slave (DMS) dual-stage servo system can be bypassed and hence its sensitivity peak will be greatly reduced. Experimental results show that the sensitivity hump of dual-stage servo loop can be reduced to very close to unity gain. With this method, TMR would be reduced without compromising low frequency vibration attenuation and suppression of head off-track disturbances .

With the continual growth of areal density in HDDs, the vibration and control issues become more significant and challenging. Future research work will be focused on these areas to obtain better disturbance rejection capabilities via servo control methodologies.

List of Tables

List of Figures

Nomenclature

A/D	Analog-to-Digital
BIT	Bode Integral Theorem
BPI	Bits-Per-Inch
CMS	Coupled Master-Slave
D/A	Digital-to-Analog
DBIT	Discrete Bode Integral Theorem
DMS	Decoupled Master-Slave
DSA	Dynamic Signal Analyser
DSP	Digital Signal Processor
FEM	Finite Element Modeling
FFT	Fast Fourier Transform
FRF	Frequency Response Function
GB	Gigabyte
HDD	Hard Disk Drive
ID	Inner Diameter

LDV	Laser Doppler Vibrometer
LPF	Low-Pass Filter
LTI	Linear Time-Invariant
MA	Micro-Actuator
MB	Megabyte
NF	Notch Filter
NMP	Non-Minimum Phase
NPM	Near-Perfect Modeling
NRRO	Non-Repeatable Run-Out
OD	Outer Diameter
ODS	Operating Deflection Shapes
PAS	Phase Assigned Spectrum
PI	Proportional-plus-Integral
PID	Proportional-plus-Integral-plus-Derivative
PES	Position Error Signal
RLS	Recursive Least Squares
RPM	Revolutions-Per-Minute
RRO	Repeatable Run-Out
SD	Sensitivity Disc
SISO	Single-Input-Single-Output
SLDV	Scanning Laser Doppler Vibrometer
STW	Servo Track Writing
TMR	Track Mis-Registration
TPI	Tracks-Per-Inch
VCM	Voice Coil Motor

Chapter 1

Introduction

In today's information explosion era, HDDs have become a cheap and important source of non-volatile storage. From the first huge magnetic drives manufactured in the 1950s to the compact drives today, HDDs have come a long way and definitely caused a dramatic growth in computer technologies. Today, this humongous capacity and high transfer rate commodity becomes an indispensable tool for many home and industrial electrical products. Typical applications include but are not limited to network servers, digital cameras, refrigerators *etc.*

1.1 Technological Advances in HDDs

The first HDD appeared in 1956 was brought in by IBM's 'remote' research laboratory in San Jose [1]. The Random Access Method of Accounting and Control (RAMAC) then moved a pair of read/write heads vertically to access the desired disk and then radially to locate the desired track. This invention recorded 5 MB on large 24″ disks, with a recording density of about 2 kb/in^2 and data transfer rate of 70 kb/s [29].

The HDDs in 1960's typically measure 14″ in diameter. Since then, magnetic recording technology made vast improvements in both recording densities, size and price of HDDs. Due to vast applications of HDDs in different electronic sectors, today's HDDs have form factor of 3.5″, 2.5″, and even the 1″ microdrive. Other reasons for manufacturing smaller HDDs include reduction of power consumption and vibration from air-flow excitation.

Advancements in technologies from media, head and signal processing research have combined to give a state-of-art high recording density HDD. As of December 2002, a typical 3.5″ form factor HDD could store as much as 80 GB in one disk platter with a tremendous data transfer rate of 160 MB/s [38]. For the smaller size HDDs, it is projected that a 2.5″ form factor HDD would double its storage capacity to 360 GB in 2005 [17]. The price of HDD have also reduced considerably, with the first HDD of 10 MB costing over $100 per MB to HDD of tens GB costing less than a cent per MB nowadays. A HDD is a high precision and compact mechatronics device. A typical commercial HDD consists of a disk pack, actuation mechanisms and a set of read/write heads, as shown in Figure 1.1. The actuation mechanism is the actuator arm driven VCM, and its main function is to position the read/write head accurately to access the data recorded on the different tracks on the magnetic disks. The other major components include:

1. disks which contain data and servo address information,

2. head-suspension assembly to perform read or write actions on the disks,

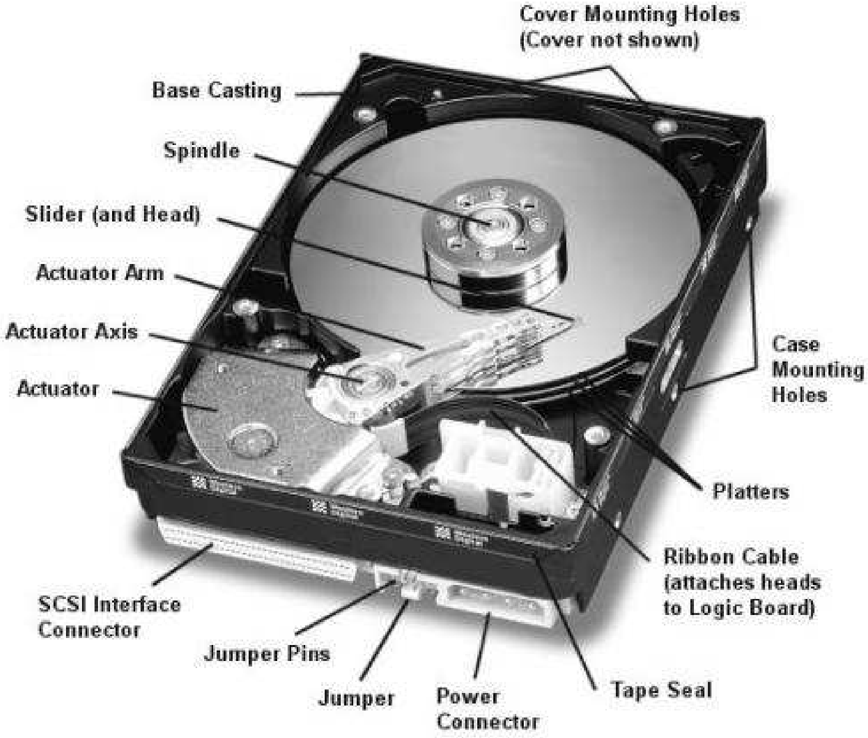

Figure 1.1: Inside a commercial HDD [28].

3. actuator assembly which contains the VCM to drive the head,
4. spindle motor assembly to make the disks rotate at a constant speed,
5. electronics card to serve as the interface to host computer, and
6. device enclosure which usually contains the base plate and cover to provide support to the spindle, actuator, and electronics card *etc.*

The disks are mounted and spun by the spindle motor. The read/write heads are mounted at the tip of the actuators protected by the sliders. Due to the amount of air-flow generated by the high speed disk rotation, a very thin air bearing film is generated and hence the head-slider can float on the disks instead of contacting them.

In a typical operation, the HDD electronic circuits receive control commands from the host computer and the control signals are processed in the on-board Digital Signal Processor (DSP). The actuator on receiving the control signal will then move and locate the read/write heads to the target locations on the disks for the read/write process to take place. During this process the Position Error Signal (PES) and the track numbers are read from the disk for feedback control.

A common measure of improvement in HDD technology is areal density, which is the amount of data stored in one square inch of disk media. It may be calculated by the multiplication of TPI and linear density BPI (Bits-Per-Inch). As technology advances, larger capacity HDD coupled with faster data transfer rate is desirable. Areal density increase are required to satisfy the demand for larger capacity HDDs. Since 1995, it has been growing by 60$\sim$100 % per year and this trend is likely to continue, if not accelerate [1]. With more data being packed into a smaller space, servo positioning during data access operation in spite of larger amounts of windage disturbances from faster disks becomes a challenge for HDD servo systems.

1.2 HDD Servo System

User data is recorded as magnetic domains on the disks coated with magnetic substrates in concentric circles called tracks. The typical HDD servo system consists of two types, namely the dedicated servo and embedded servo (or sector servo). The dedicated servo uses all the tracks on one disk surface of an entire disk pack to store servo information and is used in older generations HDDs. Currently, most HDDs employ the embedded servo method which divide the track into both storage of user data and servo information. Embedded servo is used as current HDDs have less disk platters. Furthermore, the non-collocated sensing and control in dedicated servo method introduces unacceptable manufacturing cost and noise in the HDD servo control loop. Using embedded servo, the encoded position in servo sectors can be demodulated into a track number as well as the PES, which indicates the relative displacement of the head from the center of the nearest track.

In general, there are three modes of operation for the HDD servo system. The first mode is the track seeking mode *i.e.* to move the read/write head from the initial track to the target track within the shortest possible time. Using the track number, the servo controller can locate the read/write head to the desired track during track seeking.

Next, it is the track settling mode. This process occurs once the actuator is less than one track pitch away from the target track. Due to the initial conditions of the actuators, the read/write head will be oscillating about the target track during the transient period. The track settling controller should hence guide the read/write head to be within a certain variance and tolerance with the center of the target track.

Finally, the head is maintained on the designated track with minimum error during the track following mode. The same error signal PES is used to maintain the head on the track during track following. In this mode, the main objective of the track following controller is to stay as close to the center of the track for the read/write operation to take place, in spite of the presence of external disturbances and measurement noise. The track following process has to effectively reduce TMR, which is used to measure the offset between the actual head position and the track center. During track following, TMR can also be defined as the 3σ value of PES.

In all, improving positioning accuracy is essential in order to achieve a high recording density. As TPI continues to increase with decreasing track width, external disturbances affecting the HDD servo system in all modes of servo operation become significant in achieving higher TPI.

1.3 Motivation of Dissertation

As the global demand for higher computational power increases, there is a corresponding need for better data storage devices to meet the demands of the information explosion era. HDD technology has been striving for larger data capacity and faster data transfer rate, which brings about the amazing improvement of track density and disk spin speed. Currently, it is reported that the track density would exceed 150 kTPI [63] and the disk spin speed would be 15000 rpm (revolutions-per-minute) [24]. The narrower track width requires ultra-high positioning accuracy in HDD servo system. The faster disk revolution would cause much stronger air turbulence [22], which makes the positioning task even more challenging.

For such a high TPI number and fast disk rotation speed, it is necessary to develop a high bandwidth servo system with good disturbance rejection. However disk platter vibrations, being one of the main sources of mechanical disturbances, are amplified by the closed-loop servo control system. As such, the servo loop actually amplifies head off-track caused by disk fluttering [19]. This becomes a challenge for achieving the required TMR budget and limits the achievable TPI.

As such, if the amplitude, frequency and phase from the mode shapes of disk platter vibrations are known, designing the closed-loop servo system becomes more meaningful. The peak of the sensitivity function where disturbances into the servo system are amplified can be shifted by proper controller designs to avoid the spectra of disk vibrations. If possible, the peak of the sensitivity function should be further reduced or suppressed to avoid any amplifications at all. TMR in track following mode would be vastly reduced not only by higher servo bandwidth but less amplification, even attenuation of high frequency disturbances.

1.4 Contributions and Organization

This dissertation concentrates on the study of disk platter resonances which is a great contributor to mechanical disturbances. Furthermore, as output disturbances affect PES (hence achievable TMR) via the sensitivity transfer function, a study is done to prevent the hump in the sensitivity transfer function which actually amplifies output disturbances in the HDD servo system. A new control strategy using dual-stage actuation is proposed to reduce the sensitivity hump.

The original contributions of this dissertation are as follow:

1. The mode shapes of a stationary disk at natural frequencies are captured. Using a Scanning Laser Doppler Vibrometer (SLDV), the entire disk surface is scanned non-obtrusively and the out-of-plane velocities and displacements of the disk vibrations are picked up. The software package in the SLDV reconstructs the mode shapes for animation and verification with theoretical modes obtained from Finite Element Modelling (FEM) is done.
2. On obtaining the disk vibration data in time and frequency domain, natu-

ral frequencies and vibration amplitudes are regressed on rotation speed in rpm. The effect of spindle imbalance on disk vibrations is briefly discussed. A simulation block considering effects of disk vibration is constructed and augmented with other noise and vibration models in [11] for use in designing servo controllers.

3. Using Discrete Bode Integral Theorem (DBIT) described in [12], the dual-stage servo control sensitivity limitation is found to be bounded by relative degree of the micro-actuator model. A novel method of accurately obtaining model inverse in sampled-data systems is proposed. The model inverse is premultiplied to the PZT micro-actuator and this method is termed "Near Perfect Modelling" (NPM), which is only applicable to the PZT micro-actuator due to its in phase characteristics and zero relative degree at low frequencies. NPM is not applicable to the VCM on the other hand due to causality of the digital controller to be implemented.

4. A low relative degree controller (first-order lag) is proposed to further suppress the sensitivity hump, which is apparent from inspection of the dual-stage open loop. The impact on the traditional dual-stage open loop shapes and complementary sensitivity transfer function using this type of controller will be reviewed. The effects of different sampling rate for disturbance rejection are also briefly discussed.

The rest of the dissertation is organized as follow:

- Chapter 2 describes the fundamental analysis of a HDD servo control loop and the basic limitations of a dual-stage HDD servo system.

- Chapter 3 studies the effect of disk platter resonances and captures the dynamic disk mode shapes, summarizing with a disk fluttering simulation model.

- Chapter 4 presents the different control topologies used in dual-stage HDD servo systems.

- Chapter 5 investigates the feasibility of suppressing sensitivity hump in dual-stage servo systems for disturbance rejection. Experimental results show the effectiveness of the new design methodologies on disturbance suppression and even attenuation.

- Chapter 6 summarizes the findings and results of this dissertation and some possible future research directions are presented.

Chapter 2

HDD Servo Control Loop

Currently, HDDs uses digital control with the help of fast DSPs (Digital Signal Processors). To enable better disturbance rejection and servo control, the sources of disturbances and noises should be modelled and known for this sampled-data system. Figure 2.1 shows the different sources of disturbances in the HDD servo control loop, which can be classified as the following:

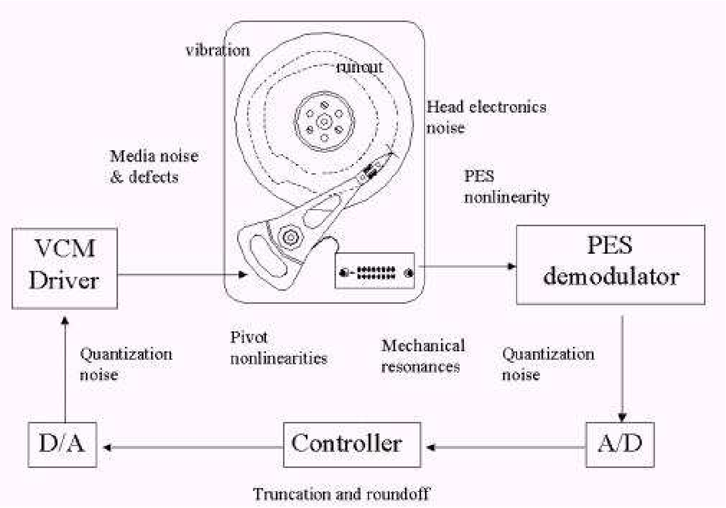

Figure 2.1: Sources of disturbance and noise in HDD servo control loop.

1. Input disturbance $d_i(s)$: Power amplifier noise, D/A (Digital-to-Analog) quantization error, pivot bearing friction, flexible cable torque, windage induced vibrations etc;
2. Output disturbance $d_o(s)$: Suspension vibrations, disk fluttering and media defects etc;
3. Noise $n(s)$: PES demodulation noise and A/D (Analog-to-Digital) quantization error etc.

The HDD PES is the error signal between the read/write head and the disk track center. The PES consists of two components : one component locked to spindle speed and phase known as the RRO (Repeatable Run-Out) and the other is the NRRO (Non-Repeatable Run-Out). RRO is synchronous to disk rotation and its harmonics while NRRO includes broad band white noise and some narrow band coloured noise without steady phase.

The measured PES is the only feedback signal to the HDD servo control system. Modelling the HDD servo system with PES as input, the following block diagram representation can be obtained:

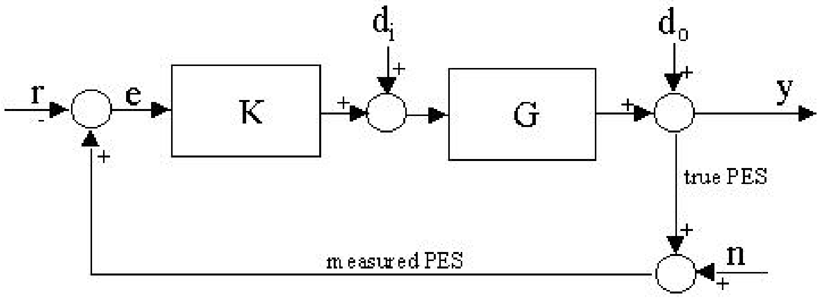

Figure 2.2: Block Diagram of HDD servo control loop.

and measured PES is given e. Assuming the open loop transfer function is given by $L = GK$, the following important equations for sensitivity function S, complementary sensitivity function T and measured PES with input disturbance d_i, output disturbance d_o and noise n can be obtained:

$$\begin{aligned} e &= y - r \\ &= -Sr + -SGd_i - Sd_o + Tn \qquad (2.1) \\ S &= \frac{1}{1+L} \qquad (2.2) \\ T &= \frac{L}{1+L} \qquad (2.3) \end{aligned}$$

The above equations hold for both continuous time and discrete time. It can be seen from equation (2.1) that a small S and T is ideal if a small e is required. In the next section, some general constraints of controller design on S and T will be discussed.

2.1 General Constraints

In a standard unity negative feedback configuration, there exists control conflicts and unavoidable trade-offs between attenuating disturbances and filtering out measurement error and noise. For good tracking performance and rejection of disturbances in low frequency region, good loop shaping techniques are essential to avoid large control signals. This section discusses some of the control constraints and controller design solutions with their effects on the sensitivity function in continuous time.

Using equation (2.1), it can be seen that a small $S(j\omega)$ is ideal for disturbance rejection and a small $T(j\omega)$ would be ideal for insensitivity to measurement noise and high frequency uncertainties. But due to the immediate definitions of $S(j\omega)$ and $T(j\omega)$, the following equation always holds:

$$S(j\omega) + T(j\omega) = 1 \qquad \text{for all } \omega \tag{2.4}$$

As such $S(j\omega)$ and $T(j\omega)$ cannot be small simultaneously and in particular, $|S(j\omega)|$ and $|T(j\omega)|$ cannot be less than $\frac{1}{2}$ at the same time. Fortunately, this conflict can be resolved by making one small at a frequency band and the other small at another band. This is possible as the power spectra of references and disturbances are usually concentrated in the lower frequencies while the power spectra of measurement error and noise are in the high frequency range.

At this point, knowing that $T(j\omega) = S(j\omega)L(j\omega)$ and design specifications on $S(j\omega)$ and $T(j\omega)$, one might be tempted to use a closed-loop approach to find stabilizing controller $K(j\omega)$:

$$\begin{aligned} K(j\omega) &= G^{-1}(j\omega)L(j\omega) \\ &= G^{-1}(j\omega)S^{-1}(j\omega)T(j\omega) \end{aligned} \tag{2.5}$$

A problem now arises as one has to choose among many possible combinations of $S(j\omega)$ and $T(j\omega)$ although their "shapes" are known. The properness and characteristics of plant $G(j\omega)$ are ignored and the controller $K(j\omega)$ derived via such a method might be causal.

A more common and easier solution is to use the open loop approach with $L(j\omega) = G(j\omega)K(j\omega)$. A good rule of thumb is to use high gain over low frequencies and decrease the gain as rapidly as possible after the gain crossover frequency. Cascading a large number of Low-Pass Filters (LPFs) are not admissible due to the amount of phase lag introduced by the filters. A good method is described by the authors in [15]. Using Bode's Stability Criterion, the typical magnitude shape of a compensated open loop transfer function of a negative feedback control system can be derived:

- Low frequency band : A large gain $\gg 0$ dB and descending with a slope of $-20N$ dB/dec ($N \geq 2$);
- Mid frequency or crossover frequency band : Pass through 0 dB with ≈ -20 dB/dec for stability;
- High frequency band : A low gain < 0 dB and descending with a slope of $-20N$ dB/dec ($N \geq 2$);

This method and control "solution" for the open loop transfer function L will be used for controller designs in the rest of the dissertation. In the next subsection, some controller design considerations from sensitivity transfer function analysis will be presented.

2.2 Sensitivity Analysis

The sensitivity function $S(j\omega)$ is the transfer function from output disturbance to desired output. As such, loop shaping methods put much emphasis on low frequency band to reject disturbance and enable better tracking. To reduce TMR further, the hump or peak of $S(j\omega)$ should be kept as low as possible to prevent amplification of the disturbances. The following two subsections are dedicated to the study of the behavior and limitations of $S(j\omega)$.

2.2.1 Sensitivity Disc (SD)

One loop shaping and controller design evaluation tool commonly used is the Nyquist plot. We shall look at how the open loop transfer function $L(j\omega)$ of the dual-stage servo loop and its sensitivity function $S(j\omega)$ are related on the Nyquist diagram. Figure 2.3 shows two typical Nyquist curves $L_1(j\omega)$ and $L_2(j\omega)$.

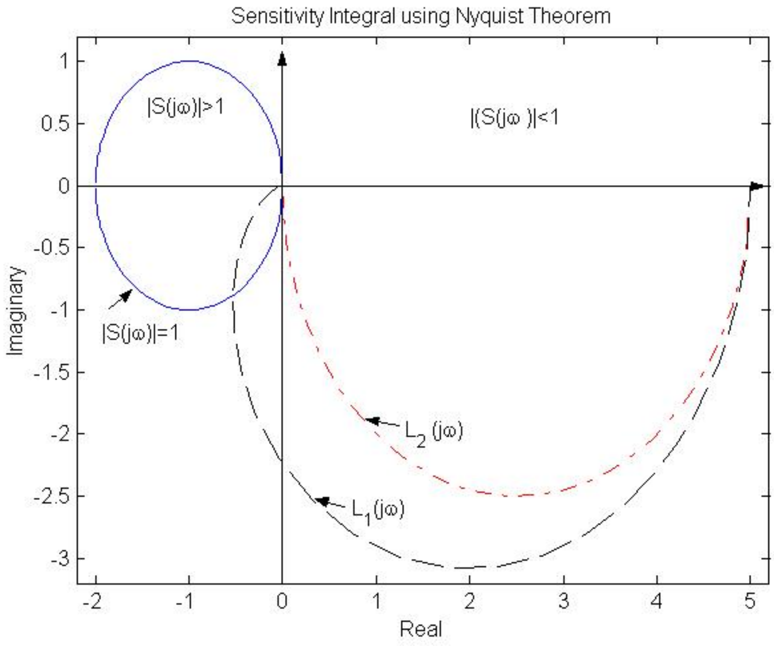

Figure 2.3: Nyquist Plot.

Since $S(j\omega) = \frac{1}{1+L(j\omega)}$ with $1 + L(j\omega)$ as the output return difference equation, the locus of $|S(j\omega)| = 1$ can be plotted as a unit disc with center at the critical point $(-1 + j0)$. We define this disc as "Sensitivity Disc" (SD). A $L(j\omega_-)$ outside SD will hence yield $|S(j\omega_-)| < 1$ and a $L(j\omega_+)$ inside SD will yield $|S(j\omega_+)| > 1$ for some frequencies ω_- and ω_+. $L(j\omega)$ touching the SD corresponds to unity gain or 0 dB on the Bode Diagram. $|S(j\omega)|$ is the reciprocal of the distance of $L(j\omega)$ to critical point $(-1 + j0)$.

As such, it can be seen from the example in Figure 2.3 that $L_2(j\omega)$ will have no hump in the sensitivity function. $L_1(j\omega)$ on the other hand cuts the SD for some $\omega \geq \omega_+$ and approaches the origin with phase angle more than $-\frac{\pi}{2}$. Negative feedback actually increases the sensitivity hump rather than decreases it at these frequencies.

With these ideas in mind, we will design our controllers to make $L_D(j\omega)$:

1. far from and not touch SD. If this is not possible, make $L_D(j\omega)$ avoid SD where the frequency spectra of the disturbances are concentrated;
2. approach the origin at $-\frac{\pi}{2} \leq \angle L_D(j\omega) \leq \frac{\pi}{2}$ as $\omega \to \infty$ so that SD is avoided. If this is not possible, make $|L_D(j\omega)| \approx 0$ at these frequencies;
3. do not encircle $(-1 + j0)$ clockwise for stability.

These tools and design considerations are valid for discrete time systems for frequencies below the Nyquist frequency f_s.

2.2.2 Bode Integral Theorem

Bode Integral's Theorem was initially derived for systems with non-minimum phase zeros or even unstable poles. In such systems, the total area of the sensitivity function will be a positive value making it impossible to reduce the hump for disturbance rejection. This is intuitive due to the extra phase lag contribution compared to their stable counterparts, leaving a smaller phase margin. Hence much feedback is used for stabilization in addition to sensitivity reduction.

In this section, the simplified Bode's Integral Theorem for continuous and discrete systems are presented for stable plants. These applications are brought to HDD dual-stage servo systems as HDDs are sampled data systems with digital controllers. Both the VCM and secondary actuator are usually modelled with stable transfer functions. The VCM has a double-integrator in its low frequency range and hence the relative degree (*i.e.* difference in order between the denominator and numerator of the transfer function, v) is $v \geq 2$ while that of the PZT micro-actuator's relative degree is $v \leq 1$ depending on modelling and the frequency range of interest.

Theorem 2.1. *Continuous Bode's Integral Theorem [60]*
A continuous Single-Input-Single-Output (SISO) Linear Time Invariant (LTI) system has the stable open loop transfer function $L(j\omega)$. The sensitivity function of the unity negative feedback system is $S(j\omega) = \frac{1}{1+L(j\omega)}$. If the closed-loop system is stable, then

$$\int_0^\infty \ln |S(j\omega)| \, d\omega = -\frac{\pi}{2} K_s, \quad K_s = \lim_{s \to \infty} sL(s) \tag{2.6}$$

When $v \geq 2$, $K_s = 0$ and hence total area under the sensitivity function. For $|S(j\omega)| < 1$ over some frequency, then a necessary condition is that $|S(j\omega)| > 1$ over another frequency range, causing a hump. This phenomenon is termed as "waterbed" effect. For discrete time systems, the Bode's Integral Theorem and their conclusions are slightly different:

Theorem 2.2. *Discrete Bode's Integral Theorem [42]*

A discrete SISO, LTI system has the stable open loop transfer function $L(z)$*. The sensitivity function of the unity negative feedback system is* $S(z) = \frac{1}{1+L(z)}$*. If the closed-loop system is stable, then*

$$\int_{-\pi}^{\pi} \ln\ |S(e^{j\phi})|\ d\phi = 2\pi(-\ln|K_z + 1|), \quad K_z = \lim_{z\to\infty} L(z) \tag{2.7}$$

and $\phi = \omega T$ *and* T *is the sampling rate.*

Now when $v \geq 1$, $K_z = 0$. This is the waterbed effect. However, when the relative degree of $L(z)$ is 0 with $K_z < -2$ or $K_z > 0$, then $\int_{-\pi}^{\pi} \ln\ |S(e^{j\phi})|\ d\phi < 0$. This implies that some loop shaping technique is possible and may not be bounded by the "waterbed" effect. Proper controller designs can be employed to bypass this phenomenon and will further explored in later chapters.

2.3 Summary

In this chapter, the sources of disturbances and noise into the HDD servo system are presented. The HDD servo system is then modelled as a unity feedback servo control system driven by PES e. The limitations and constraints on the servo control system are also investigated. Some useful controller design methodologies using an open loop solution shape and the SD are also discussed. Finally, the Bode's Integral Theorem which limits what achievable sensitivity in a HDD servo system theoretically is reviewed both for continuous time systems and discrete time systems.

Chapter 3

Disk Platter Resonances

In the previous chapter, it can be seen how output disturbances affect the PES and contribute to TMR, limiting the achievable TPI. However, the rotation speed of the spindle motors are rapidly increasing to reduce rotational latency for faster data transfer rate. This trend of rpm increment causes larger disk platters vibrations caused by air flow excitation [40], eccentricities of the disk-spindle assembly and electro-magnetic forces. This chapter provides a systematic and in-depth study of disk platter resonances and vibrations.

3.1 Background

The trend of data storage capacity has grown more than 100% every year. This trend of technological improvement requires a high track density coupled with a good track following controller to reduce TMR. At the same time, the disk-spindle spin speed also increases rapidly to improve throughput. As spin speed increases, the disk platter resonance phenomenon becomes more serious and dominates the contribution to TMR.

The mechanical disturbances due to disk platter resonances are not new to the HDD industry. In the past however, the effects of these disturbances are usually neglected because of the lower spindle rotation speeds. Also, disk vibration is axial and non-repeatable by nature. As such, little is known on the frequency spectra of these signals and their effect on head/slider off-track. Compensation is also not possible as the phase of the vibration signal is random.

In recent years, the effect of disk fluttering on TMR and the effect of different substrates on disk vibrations are studied in [39][40]. The author proposed to approximate the PES contributed by disk vibration by bandpassing overall PES in a frequency range where large disk flutter modes appear in the PES spectra. This approach is inaccurate as PES in this frequency range also comes from actuator's mechanical resonances and electrical noise from the PES measurement and demodulation channel.

Some investigations are done to characterize disk platter resonances and their impact on head/slider off-track. The authors in [4] investigated disk flutter magnitude with respect to the radius of the disk and modelled the disk flutter vibration amplitude as a linear function of disk radius. They also concluded that probability density function of the disk vibration amplitude is very close to Gaussian while the vibration peak value has a Rayleigh distribution. More recently, the authors in [27] proposed a method to reduce disk vibration by altering the air flow path inside an enclosed HDD. A good point to note is that in their study, they proposed a closed form model to convert disk flutter vibrations in axial direction to real head/slider off-track. This extra information allows possible compensation by narrowing down the frequency spectra of disturbances from disk vibrations, but still the essential phase information is unknown.

A theoretical approach is taken by the authors in [46][47]. They proposed useful mathematical models to explain and predict natural frequencies of the disk-spindle system with Rayleigh dissipation function and Lagrange's equations. Their study however, did not consider the disk-spindle assembly under operating conditions *i.e.* with air flow excitation. The negative impact of disk vibrations on overall PES as TPI increases are then projected in [19] and a simple formula to convert axial vibrations to head/slider off-track is presented.

In this chapter, the natural modes of an annul disk used in current HDDs are first characterized using FEM (Finite Element Modelling) analysis and SLDV (Scanning Laser Doppler Vibrometer) measurements. After decoupling the repeatable and non-repeatable axial vibrations, a RLS (Recursive Least Squares) algorithm is implemented to identify natural frequencies and vibration amplitudes of forward and backward travelling waves of balanced and imbalanced disks based on rotation speed in rpm. The effect of imbalance in construction of the hub of the spindle motor is also briefly discussed. With these data and the geometric model derived in [19], the actual head off-track displacement is projected in rpm. Coupled with the identification results, a disk fluttering vibration model is built for future simulations and designs of track following servo controller.

3.2 Mode Shapes

In this section, the mode shapes of a 0.8 mm thick Aluminium disk are simulated with FEM and compared with experimental results captured with SLDV. The main idea of modal testing is to construct a mathematical model of the vibrational properties and behavior of a structure through experimental means. Theoretical approaches via FEM seeks to solve complex mathematical equations to find eigenvalues and eigenvectors of the modes. Experimental approaches seek to capture natural frequencies and orthogonal mode shapes instead.

The nomenclature used in the rest of the chapter to characterize the disk vibrations is identical to those used in [39][40]. Each vibration mode of the disk has m nodal circles and n nodal diameters and is designated by (m, n). An annular plate clamped at the ID (Inner Diameter), such as the disk platter in a HDD, has similar mode shapes. The relationship between the modal indices m and n and the mode shape of a simply supported circular lamina is shown in Figure 3.1.

3.2.1 Simulation Results

With a 0.8 mm thick Aluminium disk, an FEM analysis is done on the disk with its ID constrained from movement. The simulation results in Figure 3.2 show the natural frequencies and mode shapes during static conditions *i.e.* when the disk is mounted on a stationary spindle motor.

The first four dominant $(0, n)$ modes are displayed alongside with their respective natural frequencies of disk platter resonances.

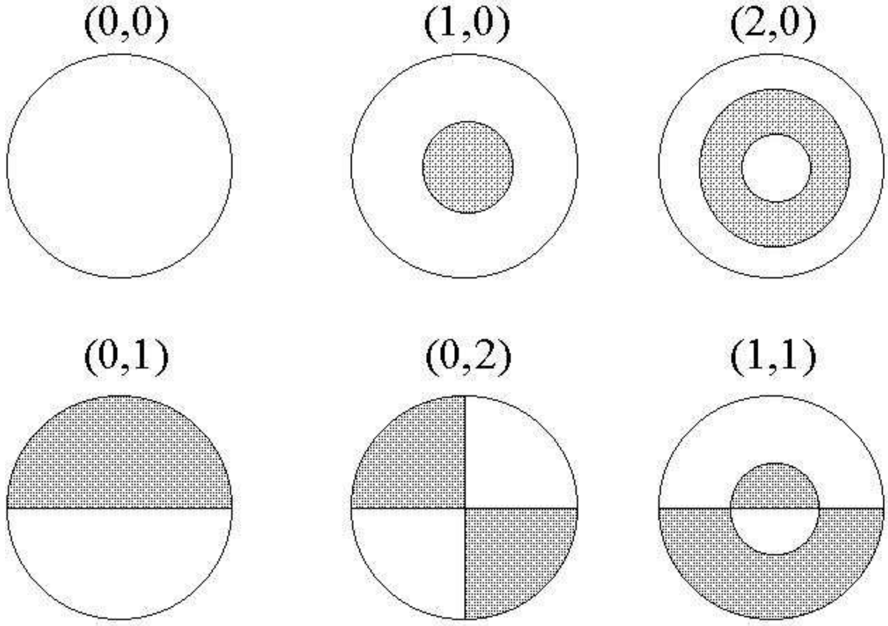

Figure 3.1: Nodal circles and diameters of a disk.

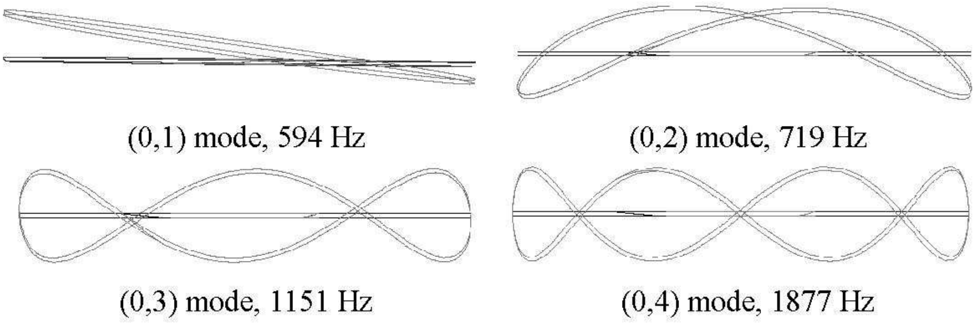
(0,1) mode, 594 Hz
(0,2) mode, 719 Hz
(0,3) mode, 1151 Hz
(0,4) mode, 1877 Hz

Figure 3.2: Simulated mode shapes and natural frequencies of a stationary disk.

3.2.2 Experimental Setup

The experimental setup is shown in Figure 3.3. For a stationary disk, an impact hammer (connected to a current amplifier to trigger the SLDV) is used to excite the natural frequencies of the disk at its Outer Diameter (OD) and the mode shapes can then be captured. In this part of the experiment, the disk modes are excited using an impact hammer when the disk is not spinning. Hammer excitation is used as it is a fast method for small homogeneous structures [18].

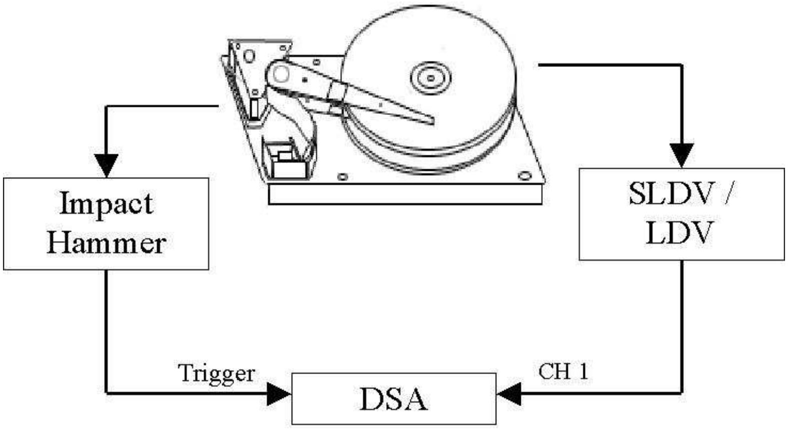

Figure 3.3: Experimental setup.

The SLDV setup includes a compact scan head, data management system and software for control of scanners, data processing and various spectra display [45]. The SLDV can capture the mode shapes and natural frequencies of a stationary or spinning disk, scanning the entire disk and non-obtrusively measuring the out-of-plane velocity and displacement of vibrations of the disk in both static and rotating conditions.

In previous works [39][40][46][47], a point by point measurement of the disk at its OD with a LDV or capacitance probe is employed and the data is then transferred to MEScope or other modal analysis software package for calculation of relevant parameters (natural frequency and mode shape *etc.*). This method enables only mode shapes of the type $(0, n)$ to be measured and displayed. The mode shapes for each natural frequency can then be easily captured when the disk is excited by an impact hammer.

However with the SLDV, the advantages of non-contact laser vibrometry together with modal reconstruction is incorporated into a single automated turnkey package [45]. It allows quick data logging and gathers complete calibrated data from an entire disk surface. The modal analysis software package in-built in the SLDV allows a fast and accurate visualization of disks vibrational characteristics. The sophisticated data validation and checking algorithms work with real-time data and ensure the frequency measurements are acquired at every scanned point with desired resolution. Using a SLDV, the Operating Deflection Shapes (ODS) of the spinning disk can also be captured. The SLDV can also capture the mode shapes and natural frequencies of non $(0, n)$ modes [45]. Dissimilar to static modes shapes in which Frequency Response Functions (FRF) using input-output relations are used, ODS are determined by the vibration patterns of the structures under operating conditions without any excitations.

3.2.3 Experimental Results

With the disks mounted on the spindle motor into the HDD fixture, the FRF can now be easily obtained. By identifying the frequencies in the peaks of the FRF, the dynamics of the linearly independent mode shapes can be captured with the SLDV when triggered.

Using an area scan employing a series of straight line scans done at the frequencies at the peaks of the FRF, spatial discrete data to describe the mode shapes of planar objects can be obtained. The mode shape surface can be reconstructed with the the modal analysis software package in-built in the SLDV. The modal analysis software allows each set of polynomial coefficients V_n to be fitted by a polynomial series [48][49] to give a 3D mode shape surface V_z given by:

$$V_z(x, y) = \sum_m \sum_n V_{mn} x^m y^n \tag{3.1}$$

with m as the number of nodal circles and n as the number of nodal diameters as indicated in earlier section.

The mode shapes captured during experiment with a stationary disk can be seen in Figure 3.4. These results are reported earlier in [44]. The theoretical natural frequencies and experimental natural frequencies tally closely. Also the mode shapes at other natural frequencies are identical to those simulated.

(0,1) mode, 603 Hz

(0,2) mode, 701 Hz

(0,3) mode, 1191 Hz

(0,4) mode, 1887 Hz

Figure 3.4: Mode shapes and natural frequencies of a stationary disk captured with SLDV.

Table 3.1: Simulation and Experimental Natural Frequencies (Hz)

Modes	$(0,1)$	$(0,2)$	$(0,3)$	$(0,4)$
Experiment	603	701	1191	1887
Simulation	594	719	1151	1877

3.3 Time and Frequency Domain Analysis

In this section, the spin-up waterfall plot of the spinning disks is obtained. The LDV is used to measure the out-of-plane displacement of the disk. By focusing the laser beam onto the OD of the disk, the time domain signals and power spectra of the vibrations can be calculated with the DSA. The behavior of the disk platter spinning at different rpm is observed. Taking readings from 3000 rpm to 16000 rpm in steps of 1000 rpm, the amplitude-modulated displacements of the vibrations are obtained. No external excitation was used.

3.3.1 Time Domain Analysis

The disk axial displacement signal is obtained in time domain. After detrending the vibration signal, the repeatable harmonic components locked to the spindle rotating speed are identified with the following identities using the known spindle speed:

$$\begin{aligned} a\,sin\theta + b\,cos\theta &\equiv R\,sin(\theta+\lambda), \\ R &= \sqrt{a^2+b^2} \\ \lambda &= tan^{-1}\frac{b}{a} \end{aligned} \tag{3.2}$$

and RLS algorithm [14]:

$$\begin{aligned} \theta(t) &= \theta(t-1) + K(t)\varepsilon(t) \\ K(t) &= P(t-1)\varphi(t)[I + \varphi^T(t)P(t-1)\varphi(t)]^{-1} \\ P(t) &= [I - K(t)\varphi^T(t)]P(t-1) \end{aligned} \tag{3.3}$$

As such, the magnitude R and phase contribution λ due to the repeatable harmonic components can be decoupled from the time domain disk vibration signal. Repeating this procedure with the known natural frequencies of the disk, R and λ for the disk mode shapes will also be known. This simple method obtains the Phase Assigned Spectrum (PAS) of spectral ODS of the spinning disks, assuming stationarity for sequential measurements without getting involved in the complex mathematics behind the physical structures. PAS in essence is the autospectrum assigned with phase between reference and signal (or the phase of the cross spectrum). This essential information will be used for compensation which will be discussed in details in later sections.

To illustrate, the time domain signal of the disk axial vibration recorded at 12000 rpm is shown in Figure 3.5. The results after removal of repeatable components are shown in Figure 3.6. Such a methodology reduces disk fluttering to a repeatable component with known amplitude R and phase λ for possible compensation.

3.3.2 Power Spectra Analysis

A power spectra estimation is done on the time domain signal collected and also on the subtracted and detrended signal. The subtracted signal contain the non-

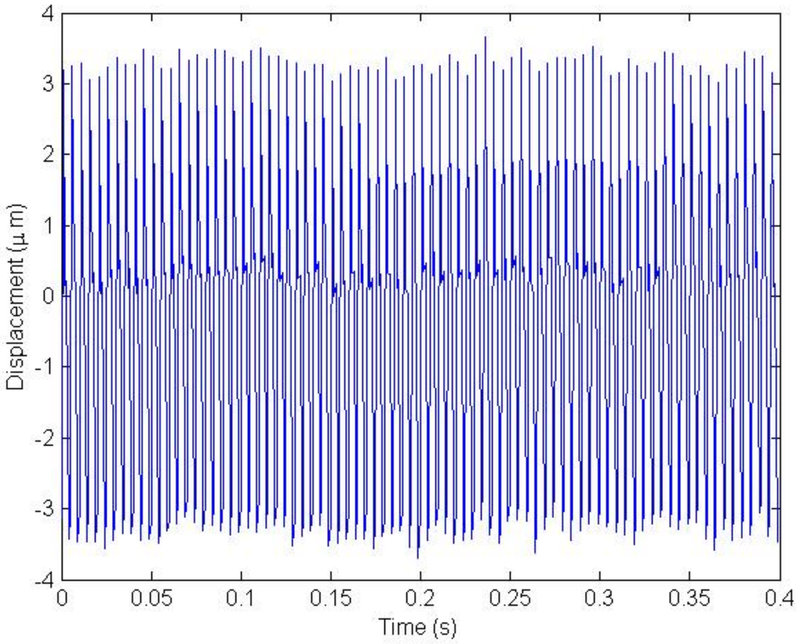

Figure 3.5: OD disk axial vibration of disk spinning at 12000 rpm (time).

repeatable information and also the vibration signals due to disk fluttering at natural frequencies.

It can be seen clearly from Figure 3.7 that the repeatable component of the disk axial displacements dominate the disk vibrations. The effects of the disk modes can now be seen in Figure 3.8. The removed DC component and the first three harmonics are also seen in Figure 3.9.

3.4 Effect of Imbalance

A small amount of adhesive material is then added onto the hub of the spindle motor of the disk pack to introduce an imbalance of 0.1 g mm to 0.5 g mm into the system assuming no initial imbalance. The experiment is then repeated. Lines are

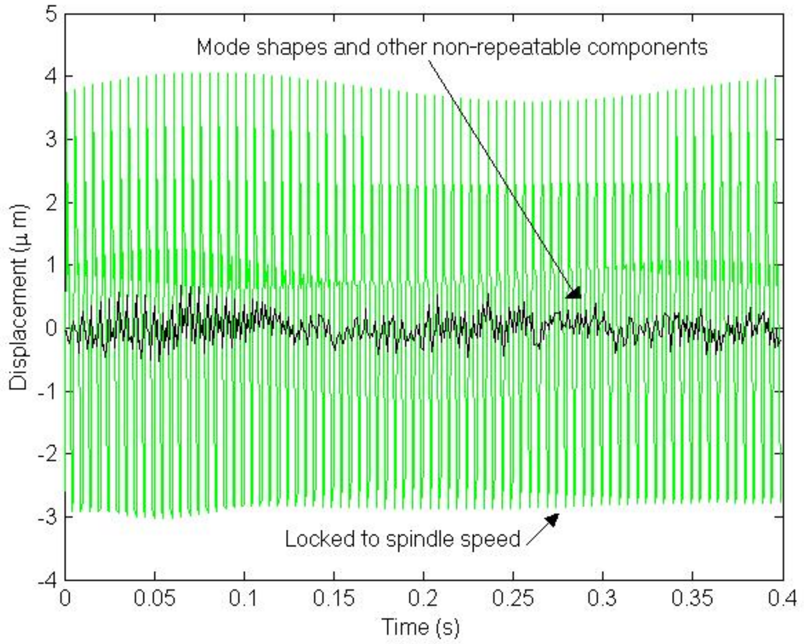

Figure 3.6: Decoupled OD disk axial vibration of disk spinning at 12000 rpm (time): Locked to spindle speed (solid); Mode shapes and other non-repeatable components (dashed-dot).

drawn and connected through the peaks for curve-fitting.

For the spindle-disk pack spinning at 12000 rpm, the 3σ axial vibration amplitude against amount of imbalance introduced is plotted and shown in Figure 3.10. The 3σ value represents a stochastic probability of 99.72% of the axial vibration within the 3σ range. As such, it can be seen easily that the imbalance has a great effect on the amplitude of vibration of the disk. As the amount of spindle-hub imbalance increases, the OD 3σ axial vibration increases significantly in an approximate quadratic trend. This implies that the disk fluttering problem is more serious as imbalance increases, and the negative impact of this imbalance can be seen on the chart as shown in Figure 3.10.

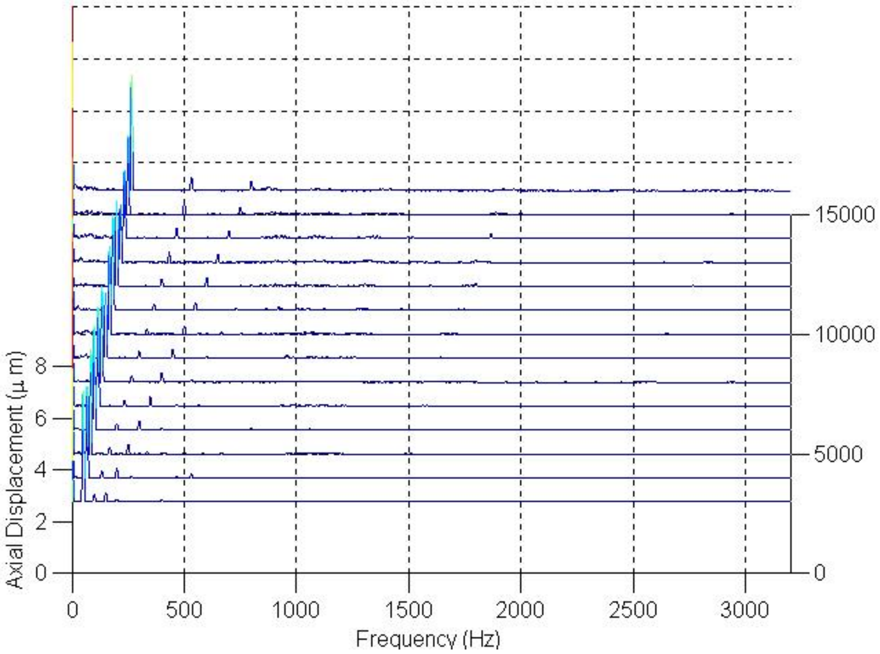

Figure 3.7: Spin-up waterfall plot without imbalance.

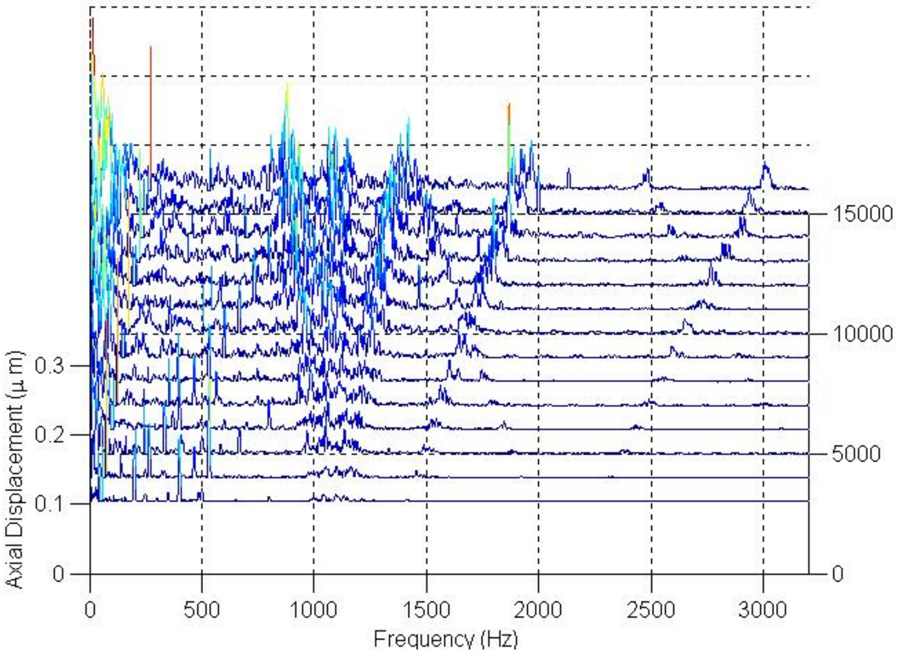

Figure 3.8: Spin-up waterfall plot with repeatable parts removed.

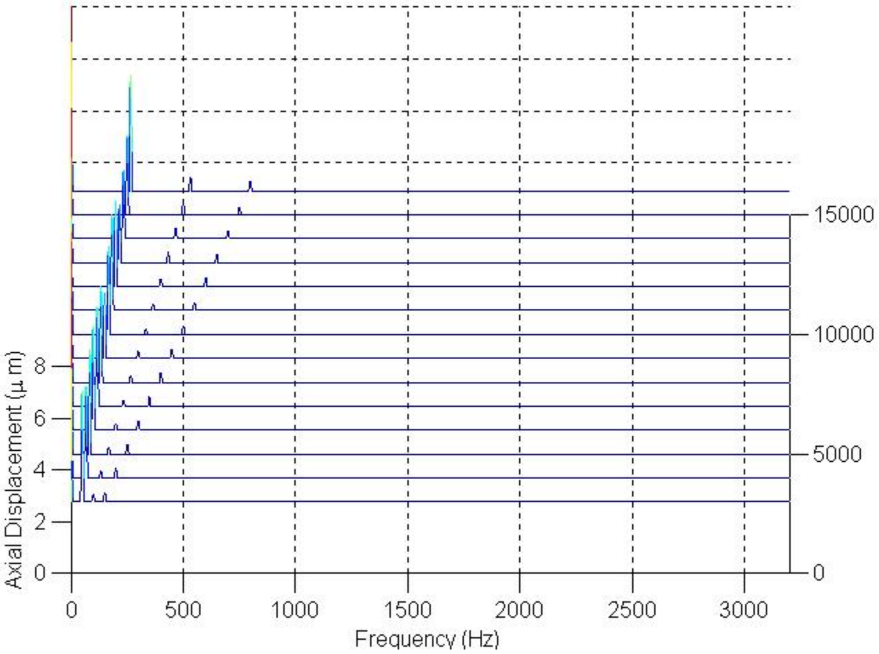

Figure 3.9: Spin-up waterfall plot of DC and first three dominant harmonics.

3.5 Natural Frequencies and Vibration Amplitudes

With the decoupled time and frequency signals of disk axial vibrations, this section aims to further predict the natural frequencies and vibration amplitudes regressed on rotation speed in rpm. This is to facilitate building of the simulation tool and the disk flutter model in later sections.

3.5.1 Natural Frequencies vs Rotational Speed

From a ground-fixed observer, the natural frequencies of a spinning disk can be described by a linear relationship [47] governed by the mode of vibration $(0, n)$.

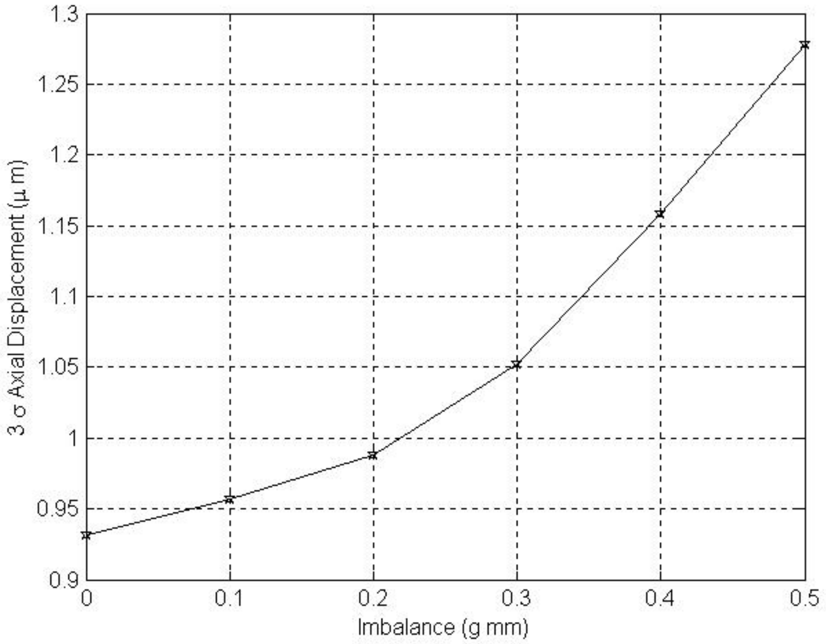

Figure 3.10: OD disk platter axial displacement amplitude (3σ) with different amount of imbalance for disk spinning at 12000rpm.

In this section, the RLS algorithm is used to determine the unknowns assuming a following linear relationship:

$$\omega_{res} = \omega_{(0,n)} + \alpha\,\Omega \tag{3.4}$$

where n is the number of nodal diameters and Ω is the rotational speed in rpm. The constant α will be determined using the RLS algorithm in equation (3.3) provided the the pseudo-inverse $\Phi^T\Phi$ is non-singular provide the excitation is sufficiently rich. The $(0,0)$ mode has no branches and the results are summarized below.

An experimental approach of determining α is more attractive than a theoretical solution due to its reliability and accuracy on extrapolation at higher rpm. This simple linear equation will be used later for disk vibration model building.

Table 3.2: α for Mode Shapes of a disk.

Modes	$(0,1)$	$(0,2)$	$(0,3)$	$(0,4)$
α	± 0.0185	± 0.0354	± 0.0512	± 0.0678

With the RLS algorithm, the unbiased estimates of the parameters can be updated when new data comes in.

3.5.2 Vibration Amplitudes vs Rotational Speed

Similarly, the amplitude of vibration can be projected and regressed on rotational speed Ω in rpm. A simple linear relationship is used in [44] as the rotation speeds are lower compared to the current experiment. For a high rotation speed such as 15000 rpm, a quadratic relationship is more accurate. Using a similar approach as above, we can derive the vibration amplitude y_v in the form of:

$$y_v = \beta_2 \, \Omega^2 + \beta_1 \, \Omega + \beta_0 \tag{3.5}$$

The RLS equation in equation (3.3) will be used again to estimate the curve of best fit. Curve-fitting will be done for the first 3 dominant harmonics of repeatable portions of the disk axial vibrations and on the various mode shapes. Knowing the frequency and phase of the mode shapes, the mode shapes are reduced to repeatable components which can be compensated by the servo control. The obtained entire list of β parameters are omitted in this dissertation.

3.6 Modelling of Disk Flutter Vibration

With the essential information derived above via an experimental approach, the axial vibration displacement and natural frequencies will be known on a predetermined rotation speed of the spindle motor in rpm. The power spectra can now be modelled as a transfer function with white noise input [11]. With this methodology, the power spectra of the axial disk vibrations can be reconstructed easily. The experimental results of a disk rotating at 12000 rpm is compared with the simulated results after modelling.

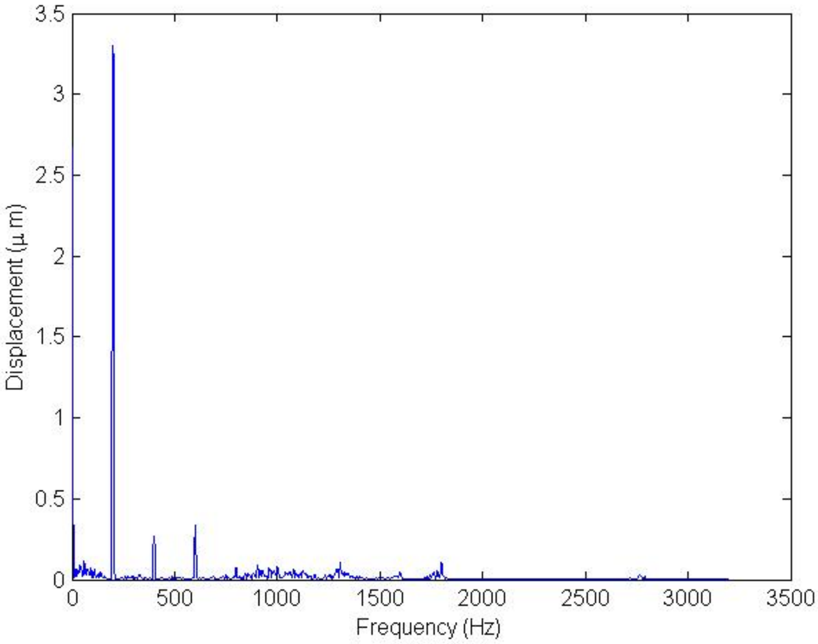

Figure 3.11: Power spectra of disk axial vibration at 12000 rpm: experimental.

The experimental disk axial vibration for disk spinning at 12000 rpm in time domain is seen earlier in Figure 3.6. The results after mathematical modelling are shown in Figure 3.13. It can be seen that the fit is good and the residual error is

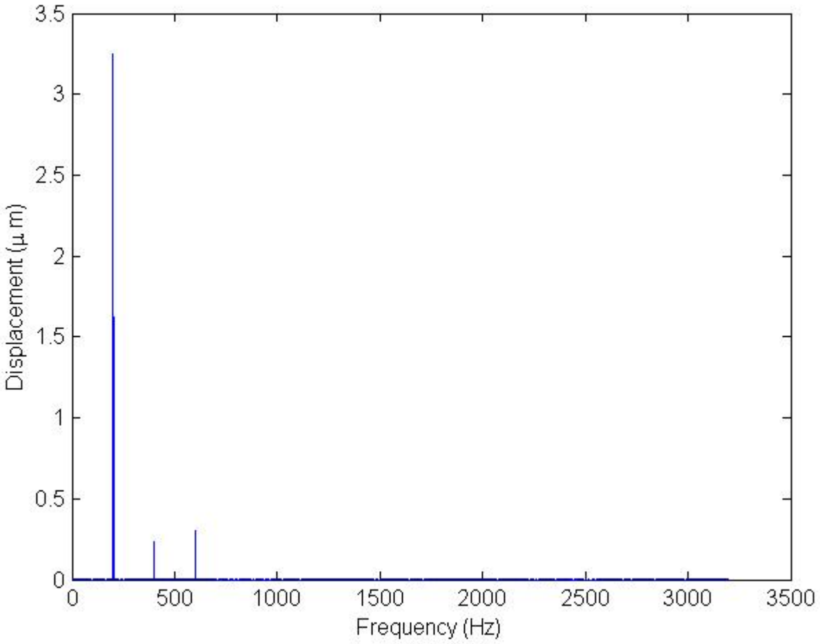

Figure 3.12: Power spectra of disk axial vibration at 12000 rpm: model.

very small. This error coincides with the unmodelled non-repeatable components and are unpredictable.

To convert the axial displacement to slider-off track, the geometric model derived in [19] is used. The geometric model averages the first 4 dominant modes of the disk resonances and approximates a direct relationship between head off-track Ot to disk fluttering magnitude h as:

$$Ot = 0.032\,h \tag{3.6}$$

Given a rotation speed in rpm and using equation (3.6), we can now convert the power spectra of the axial displacement to power spectra of the slider off-track displacement. The amplitudes R and phases λ of the repeatable components (inclusive of components locked to spindle rotation speed and mode shapes) can

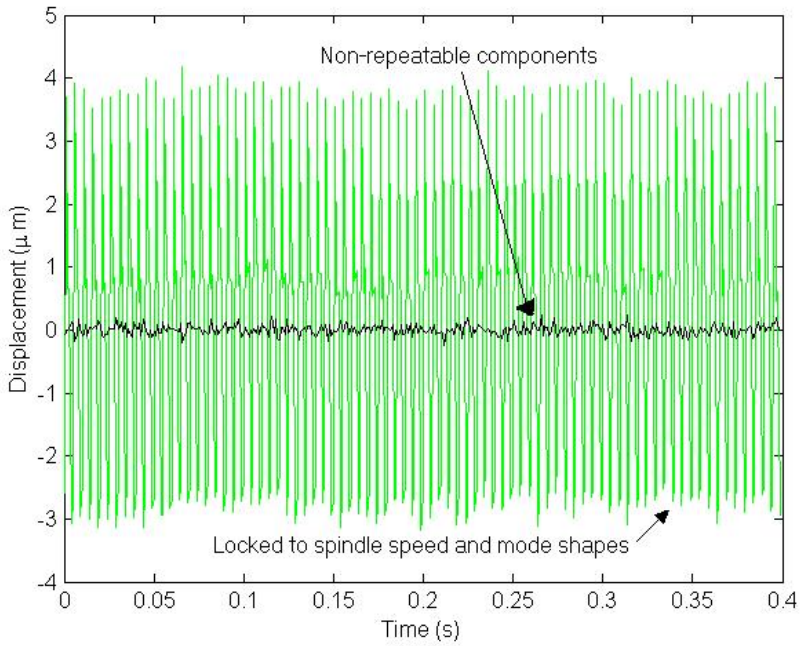

Figure 3.13: Modelled disk axial vibration of disk spinning at 12000 rpm (time): Model (solid); Non-repeatable components (dashed-dot).

be predicted and modelled.

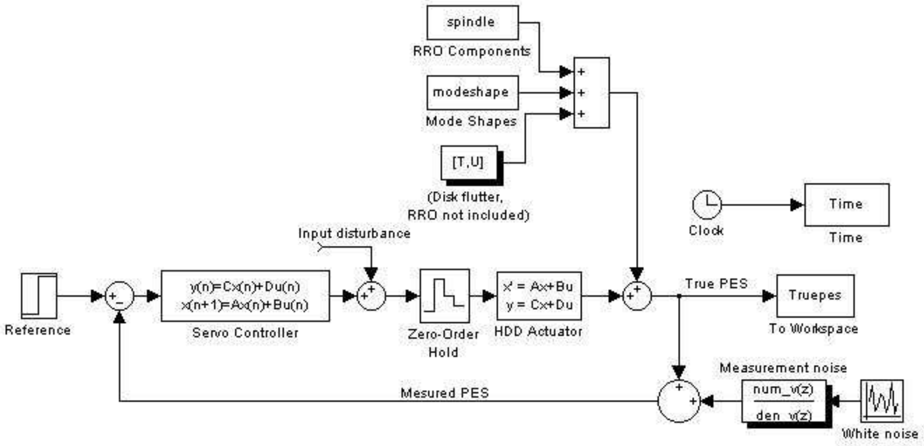

Figure 3.14: Simulation block diagram for slider off-track at 12000 rpm.

This information is very useful and can be used for simulations and servo controller designs. The SIMULINK block diagram created to simulate the effects of axial disk fluttering on slider off-track is shown in Figure 3.14. The residual baseline vibration models representing the non-repeatable components and noise models (functional block diagrams with drop shadow) are obtained from [11]. The effects of imbalance can be similarly augmented into the block by simply changing the β parameters as derived above. A possible compensation and modelling scheme for identifying PAS followed by effective active control is presented in [21].

3.7 Summary

Mechanical disturbances due to disk vibrations are one of the main contributors to TMR and they limit the achievable TPI. In this chapter, the mode shapes of a disk are captured and the natural frequencies, vibration amplitudes (and phases) on higher rotational speeds are projected based on an experimental approach. Although vibration amplitudes and natural frequencies have very complicated physics behind which depend also on the geometry of the enclosure, identification of the experimental results is used for predicting the vibration amplitudes on rotating speed. This method does not provide any insight into the underlying physics but allows the amplitude, mode shape and natural frequency of vibration to be known easily.

A time-domain disturbance model is then built on the identification results. Knowing the amplitude, frequency and mode shape of vibration is useful when considering the design specifications for the closed-loop servo system with a predetermined rotation speed in rpm. The simulation block diagram developed can be used to convert axial vibration to slider off-track, enabling a better design for track following controller. The next chapter explores dual-stage control and its disturbance rejection capabilities. It is shown in later chapters how the peak of the sensitivity function where disturbances are amplified can be avoided at the natural frequencies.

Chapter 4

Dual-Stage Actuation

Dual-stage actuation is already implemented in current optical drives and vast improvements can be seen after their successful implementations. This idea was then brought to magnetic recording technology and hence as attracted extensive attention in the HDD industry. In a HDD, dual-stage actuation is enabled via appending a small secondary actuator (usually termed micro or milli-actuator depending on size) onto the primary actuator, VCM. Improving bandwidth in a HDD servo system is a common measure of disturbance and noise rejection and hence dual-stage actuation is seen as a viable candidate for the newer generation of HDDs.

This chapter covers the modelling of VCM and micro-actuator using a frequency domain approach. Some commonly used dual-stage structures and topologies will be covered and an example of a dual-stage track-following controller will be presented.

4.1 VCM and Micro-actuators

In a HDD dual-stage servo system, the secondary actuator is of a much smaller dimension when compared to the VCM. Usually mounted on the VCM, the read/write head is then placed onto the tip of the secondary actuator. To improve servo performance, the secondary actuator should be light (low inertia) have a high bandwidth with little high frequency uncertainties. These ideal characteristics will enable the secondary actuator to cancel disturbances entering the servo control system before they affect the true PES.

However, the secondary actuators (commonly known as micro-actuators have a very small displacement range ($0.2 \sim 2\mu$m) and hence is not suitable for track-seeking operation. As such, track-seeking is done by the primary actuator VCM and the secondary actuator will be active in the track-following mode. Care has to be taken to prevent saturation of the secondary actuator which will tend to destabilize the servo loop when linear controllers are used. Nonlinear controllers can be used for short span seek of several tracks to tackle the effect of actuator saturation effectively [21].

System identification is used to identify the models required for designing of controllers (and estimators). This input-output relationship based method jumbles up the physical quantities of mass, force *etc.* into coefficients of transfer functions. Although these coefficients gives no insight into the underlying physics of the mechanisms, the transfer function approach is practical and preferred for control purposes.

4.1.1 Primary Actuator : Voice Coil Motor (VCM)

In the conventional single stage actuation found in current HDDs, the VCM is the only actuator with the read/write head mounted on the tip. Other components include a pivot (for rotary actuator), ball bearings, the arms commonly known as the “E” block, a flex cable and suspensions at the tip to carry the sliders. The VCM is harnessed in between two very strong permanent magnets commonly called the yoke. When current is passed into the coil of the VCM, force and hence displacement is transduced to move the read/write heads. A picture of a VCM consisting of the above components is shown below in Figure 4.1.

Figure 4.1: A picture of VCM.

By exciting the VCM at frequencies of interests, the displacement of the VCM at the tip of the secondary actuator is measured by the LDV non-obtrusively. Swept sine excitation from the DSA is introduced into the power amplifier and the frequency response of the VCM is captured and identified in MATLAB. A typical frequency response captured is plotted and shown in Figure 4.2.

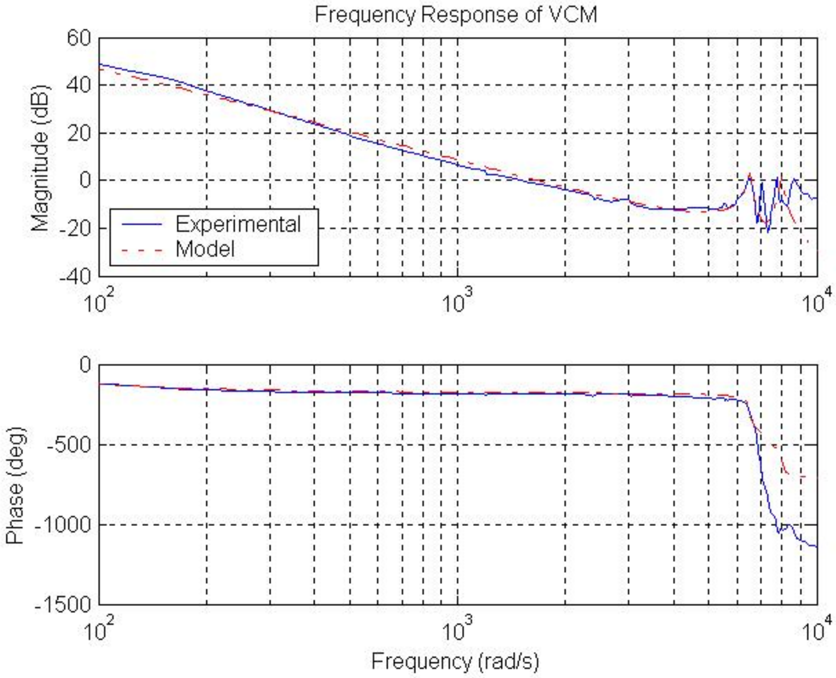

Figure 4.2: Frequency response of VCM.

With prior knowledge from physical modelling and curve fitting, it can be shown that the VCM can be modelled as double integrators with some resonant modes and anti-resonant zeros. The overall transfer function of a VCM in s-domain can be expressed as:

$$G_V(s) = \frac{K_V}{s^2} \prod_{i=1,j=1}^{m,n} \frac{s^2 + 2\zeta_j \omega_j s + \omega_j^2}{s^2 + 2\zeta_i \omega_i s + \omega_i^2} \tag{4.1}$$

with ζ as the damping ratio and ω as the natural frequency of the modes. Minimum phase zeros are sometimes included to provide some phase lift. Non-minimum phase zeros are usually ignored during the modelling process as they do not affect the closed-loop stability of the VCM. The transfer function for the model shown

Figure 4.2 is:

$$G_V(s) = \frac{1.38\times 10^8}{s^2} \prod_{i=1,j=1}^{2,1} \frac{s^2 + 2\zeta_j\omega_j s + \omega_j^2}{s^2 + 2\zeta_i\omega_i s + \omega_i^2} \tag{4.2}$$

Table 4.1: Parameters of VCM model.

	ζ	ω
i=1	0.01	$2\pi \times 6.5 \times 10^3$
i=2	-0.05	$2\pi \times 7.1 \times 10^3$
j=1	0.01	$2\pi \times 8.0 \times 10^3$

In this case, a minimum phase zero is added to match the phase.

4.1.2 Secondary Actuator : Micro-actuator

Several micro-actuator designs have been reported in recent years. Depending on the actuation mechanism, these designs can be categorized into (i) piezoelectric [52], (ii) electrostatic [16] and (iii) electromagnetic [34]. The secondary actuators can also be categorized according to their locations which include (i) suspension-based [12], (ii) slider-based [23] and (ii) head-based [16]. In this dissertation, a piezoelectric suspension-based secondary actuator will be discussed. The piezoelectric element used usually is Lead-Zirconim-Titanate ceramic (Pb-Zr-Ti). Hence, these actuators are also called PZT micro-actuators.

The suspension-based actuator is sometimes called a milli-actuator due to its mass when compared to its fellow counterparts. Piezoelectric ceramic material has high stiffness and generate large force by contraction and expansion. When actuated, the whole suspension length is moved and hence it yields a larger displacement range. PZT micro-actuators often employ the push-pull [43] or shear [33] design according to the direction of polarization of the piezoelectric materials. A picture of a PZT micro-actuator is shown in Figure 4.3.

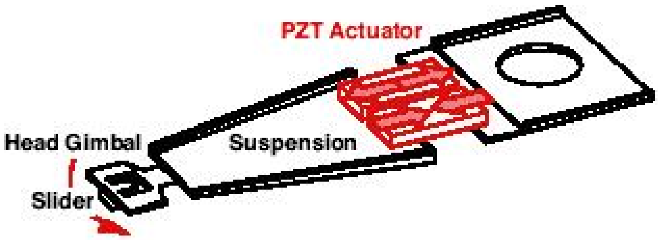

Figure 4.3: A picture of PZT micro-actuator [54].

A two strip setup of suspension-based micro-actuator can be seen in Figure 4.3. Two small parallel strips of PZT elements can be found at the base of the suspension. When a voltage is applied to these elements, one PZT strip expands while the other contracts to deflect the entire suspension. Usually, the suspension-based micro-actuator designs can yield a stroke of > 1 μm with first resonant mode in the range of 5∼15 kHz.

Using the same methodology, the displacement of the PZT micro-actuator is measured by the LDV. Swept sine excitation from the DSA is introduced into the power amplifier and the frequency response of the secondary actuator is captured and identified in MATLAB. The frequency response of the micro-actuator shown in Figure 4.3 is captured and plotted in Figure 4.4.

It can be seen that the PZT micro-actuator can be modelled as a pure gain in a

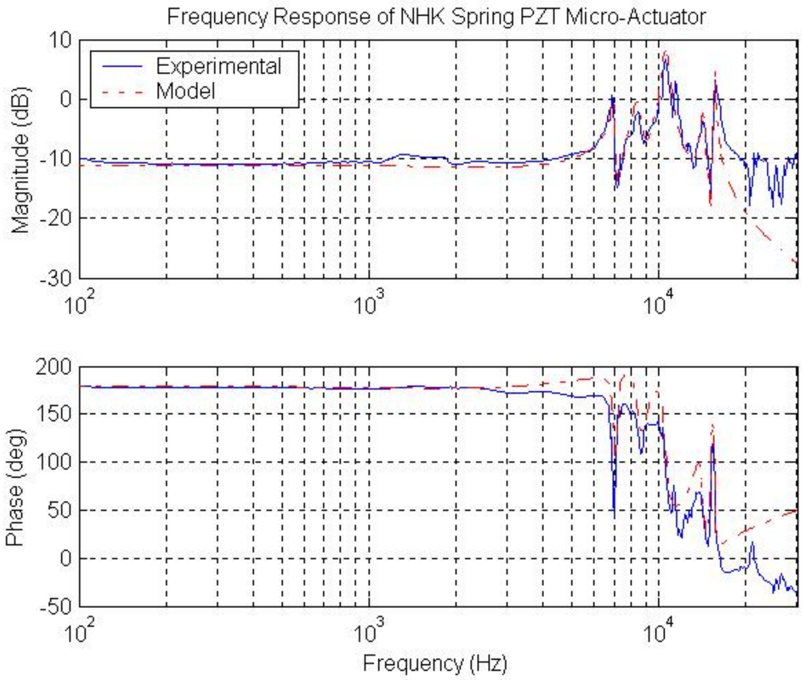

Figure 4.4: Frequency response of PZT micro-actuator.

large range of frequencies with some resonant modes and anti-resonant zeros. The overall transfer function of the PZT micro-actuator in s-domain can be expressed as:

$$G_M(s) = K_M \prod_{i=1,j=1}^{m,n} \frac{s^2 + 2\zeta_j\omega_j s + \omega_j^2}{s^2 + 2\zeta_i\omega_i s + \omega_i^2} \tag{4.3}$$

Depending on application and design specifications, the PZT micro-actuator can usually be modelled as:

$$G_M(s) = K_M \tag{4.4}$$

or

$$G_M(s) = K_M \frac{\omega_i^2}{s^2 + 2\zeta_i\omega_i s + \omega_i^2} \tag{4.5}$$

where ω_i is the angular frequency of the first dominant resonant mode of the PZT micro-actuator. These models are usually sufficient for high servo bandwidth dual-stage control designs. The transfer function for the model shown Figure 4.4 is:

$$G_M(s) = 0.005\frac{s + 2\pi \times 30 \times 10^3}{s + 2\pi \times 3 \times 10^3} \prod_{i=5,j=5}^{m,n} \frac{s^2 + 2\zeta_j\omega_j s + \omega_j^2}{s^2 + 2\zeta_i\omega_i s + \omega_i^2} \tag{4.6}$$

Table 4.2: Parameters of PZT micro-actuator model

	ζ	ω
i=1	0.015	$2\pi \times 6.991 \times 10^3$
j=1	0.013	$2\pi \times 7.192 \times 10^3$
i=2	0.035	$2\pi \times 8.451 \times 10^3$
j=2	0.055	$2\pi \times 8.893 \times 10^3$
i=3	0.025	$2\pi \times 10.542 \times 10^3$
j=3	0.090	$2\pi \times 13.550 \times 10^3$
i=4	0.020	$2\pi \times 14.196 \times 10^3$
j=4	0.010	$2\pi \times 15.066 \times 10^3$
i=5	0.006	$2\pi \times 15.588 \times 10^3$
j=5	1	$2\pi \times 25.000 \times 10^3$

A higher order model is fitted and its application will be justified in later chapters. The experimental results show better disturbance rejection and suppression and will be presented.

4.2 Dual-stage Control Topologies

In a dual-stage HDD using PZT suspension-based secondary actuator, only the relative displacement is available. Also the only measurable quantity in a real

HDD is true PES. As such, Single-Input-Single-Output (SISO) design structures are usually employed on the VCM and micro-actuator loop separately and then combine the results into a complete dual-stage loop. This method gives actual insight into the working principles of the two actuators at different frequency ranges. The different control topologies will be discussed in this section.

Assuming the following nomenclature with G_V and G_M as VCM and micro-actuator models and C_V and C_M as controllers for VCM and micro-actuator respectively. Also, L_D is the open loop transfer function of the dual-stage control loop. S_V, S_M and S_D are the sensitivity functions of the VCM loop, micro-actuator loop and overall dual-stage control loop. T_V, T_M and T_D are the closed-loop transfer functions (or complementary sensitivity functions) of the VCM loop, micro-actuator loop and dual-stage control loop respectively.

4.2.1 Dual Feedback Configuration

It is proven in [20] that the ideal configuration for dual-stage control is the dual feedback configuration. The functional block diagram of this structure is shown below in Figure 4.5. This structure needs the output of both VCM and the micro-actuator for feedback. As such, the relative displacement of the two actuators should be detected. In this structure, the micro-actuator is driven by the error signal from the VCM path and hence it makes use of the micro-actuator to further reject disturbance and eliminate position error.

The corresponding open loop, sensitivity and complementary sensitivity trans-

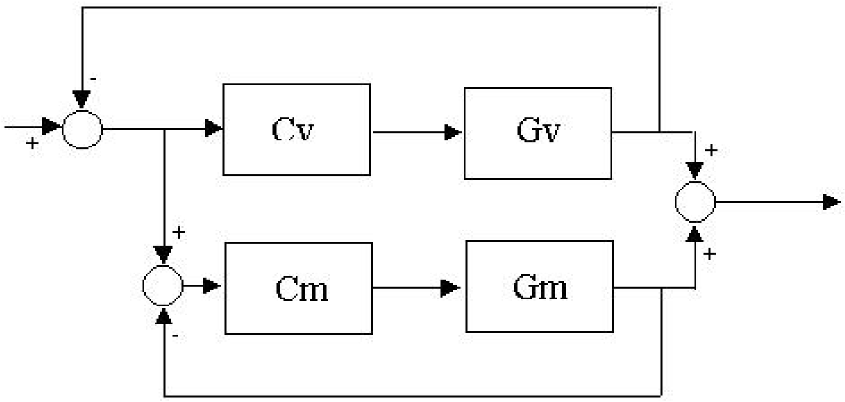

Figure 4.5: Dual feedback configuration.

fer function of the dual feedback configuration are:

$$L_D = (1 + C_M G_M) C_V G_V + C_M G_M \tag{4.7}$$

$$T_D = \frac{(1 + C_M G_M) C_V G_V + C_M G_M}{(1 + C_V G_V)(1 + C_M G_M)} \tag{4.8}$$

$$\begin{aligned} S_D &= S_V S_M \\ &= \frac{1}{1 + C_V G_V} \frac{1}{1 + C_M G_M} \end{aligned} \tag{4.9}$$

It can be seen that the crossover frequency of the dual-stage control loop is higher than that using single stage actuation. Also the sensitivity function of the dual-stage loop is the product of the sensitivity function of the VCM loop and the micro-actuator loop. This implies that disturbance suppression and rejection is more effective in the dual-stage control loop.

4.2.2 Parallel Configuration

Although dual feedback is ideal, it is not feasible in HDD servo system as true PES is the only reference. As such, the following Dual-Input-Single-Output (DISO) configuration is proposed. The functional block diagram of this structure is shown below in Figure 4.6.

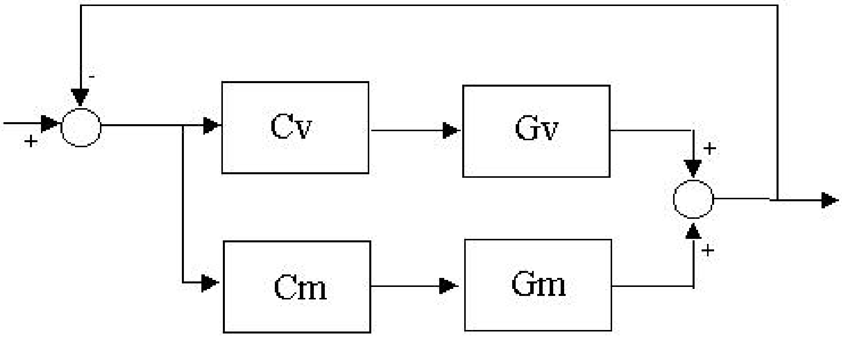

Figure 4.6: Parallel configuration.

The corresponding open loop, sensitivity and complementary sensitivity transfer function of the parallel configuration are:

$$L_D = C_V G_V + C_M G_M \tag{4.10}$$

$$T_D = \frac{C_V G_V + C_M G_M}{1 + C_V G_V + C_M G_M} \tag{4.11}$$

$$S_D = \frac{1}{1 + C_V G_V + C_M G_M} \tag{4.12}$$

The sensitivity function is similar to that of the single stage actuation with the addition of $C_M G_M$ in the denominator. Control designs in parallel structure usually end up with $|C_V G_V| \gg |C_M G_M|$ in the low frequency range and $|C_V G_V| \ll |C_M G_M|$ in the high frequency range. This implies that the micro-actuator "works" in the higher frequency range enabling disturbance rejection while the VCM functions in the lower frequencies.

4.2.3 Master-Slave Configuration

The primary advantage of a master-slave configuration is to put priority onto one actuator than the other [20], making the micro-actuator respond faster to external disturbance by being the "master" and the bulky VCM as the "slave" to compensate for slower variations in the relative displacement between the actuators.

The master-slave configuration comes in a slight variation : the Coupled Master-Slave (CMS) structure and the Decoupled Master-Slave (DMS) structure. Both configurations require a micro-actuator model as part of the VCM controller to estimate the micro-actuator output and is used to drive the VCM. The functional block diagram of the CMS configuration is shown in Figure 4.7.

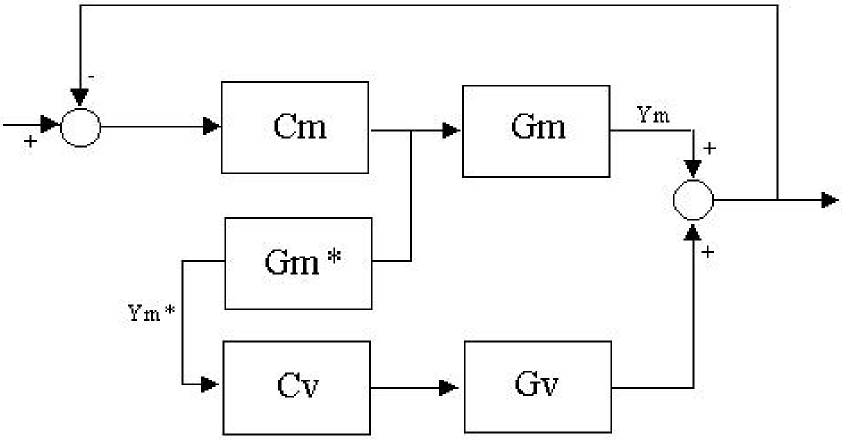

Figure 4.7: Coupled master slave configuration.

The corresponding open loop, sensitivity and complementary sensitivity transfer function of the CMS configuration are:

$$
\begin{aligned}
L_D &= (1 + C_V G_V) C_M G_M && (4.13)\\
T_D &= \frac{(1 + C_V G_V) C_M G_M}{1 + C_M G_M + C_V G_V C_M G_M} && (4.14)\\
S_D &= \frac{1}{1 + C_M G_M + C_V G_V C_M G_M} && (4.15)
\end{aligned}
$$

The functional block diagram of the DMS configuration is shown below in Figure 4.8.

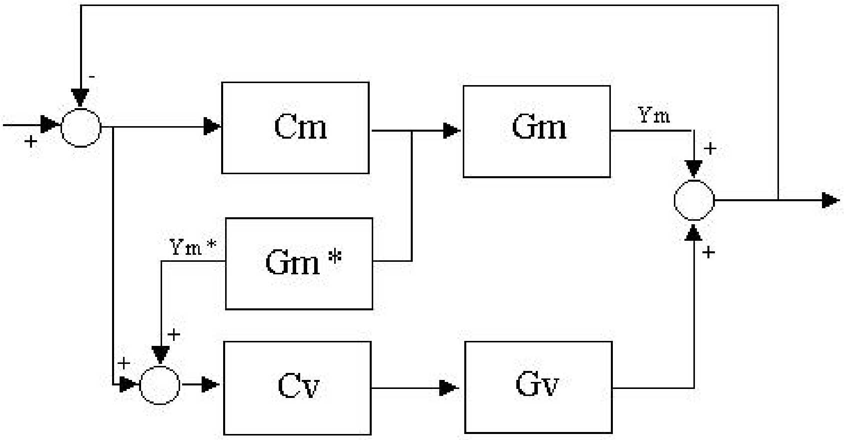

Figure 4.8: Decoupled master slave configuration.

The corresponding open loop, sensitivity and complementary sensitivity transfer function of the DMS configuration are:

$$
\begin{aligned}
L_D &= (1 + C_M G_M) C_V G_V + C_M G_M && (4.16)\\
T_D &= \frac{(1 + C_M G_M) C_V G_V + C_M G_M}{(1 + C_M G_M)(1 + C_V G_V)} && (4.17)\\
S_D &= S_V S_M && (4.18)\\
&= \frac{1}{(1 + C_M G_M)(1 + C_V G_V)} && (4.19)
\end{aligned}
$$

Note that the sensitivity function of the DMS structure is similar to that of the ideal dual feedback structure *i.e.* the product of the sensitivity function of the VCM loop and the micro-actuator loop. Obviously, the DMS design can be converted into the parallel design when the VCM controller is designed as:

$$C_V* = (1 + C_M G_M) C_V \tag{4.20}$$

The DMS scheme is more preferable to than that of the CMS (and other configurations mentioned above) as the error signal is split into two independent control loops. Implementation will be eased as the loops can be closed independently and dual-stage closed-loop stability will be ensured. Also, better disturbance rejection is enabled with the product of the individual path sensitivity functions. As such, this simple yet effective method will be employed in the rest of the dissertation.

However, the performance of the master-slave configuration depends highly on the effectiveness of the estimator. If the estimator gives an actuator output which is close to the actual displacement of the micro-actuator ($Y_M \approx Y_M^*$), then disturbance rejection capabilities and servo performance will be enhanced. This is because the difference of the sensor output and the estimated micro-actuator output gives a good estimate of the VCM output. This important observation will be further explored in the next chapter.

4.3 Example of Dual-Stage Control

Because of the limited displacement range of the secondary actuator, the actuation effort between the two actuators should be distributed properly when designing the respective controllers. An effective dual-stage loop should have the following characteristics so that the actuators will not compete with one another [30]:

- VCM should respond to correct the errors at low frequency while the secondary actuator will respond to the error signal at higher frequencies;
- Not more than 120° phase difference between the secondary actuator and VCM output at the so-called “hand-off” frequency. The typical hand-off frequency is about 400 Hz;
- VCM output should exceed secondary stage output by 20 dB below 60 Hz to prevent saturation of the secondary actuator.

The existence of structural resonant modes in both the VCM and PZT micro-actuator will not be able to meet the above criterion as the gain of the actuators are very high at resonant frequencies. These large gain at the lightly damped poles not only cause oscillations in the step response but even instability in the closed-loop servo system due to poor gain margin when the magnitude curve cuts through 0 dB again at the high frequency band.

As such, notch filters are commonly used [55] to suppress the energy (hence gain) of the resonant modes at the resonant frequencies by attenuating the signal power to avoid the excitation of the associated structural mode.

4.3.1 Notch Filter Design

This section is dedicated to the design of notch filters for use in resonant compensation. Suppose the VCM has a resonant mode at natural frequency f_R which the mode can be represented by:

$$R(s) = \frac{(2\pi f_R)^2}{s^2 + 2\zeta_R(2\pi f_R)s + (2\pi f_R)^2} \tag{4.21}$$

where ζ_R is the damping ratio ($0 < \zeta_R < 1$). An intuitive notch filter design would be:

$$NF(s) = \frac{(2\pi f_D)^2}{(2\pi f_R)^2} \frac{s^2 + 2\zeta_R(2\pi f_R)s + (2\pi f_R)^2}{s^2 + 2\zeta_D(2\pi f_D)s + (2\pi f_D)^2} \tag{4.22}$$

to ensure perfect cancellation of the resonant mode. $\sqrt{2} < \zeta_R \leq 1$ is usually chosen to replace the lightly damped poles to more well-damped ones. When $f_R = f_D$, some degradation in phase response is still apparent at the resonant frequency. A high pass notch using $f_D > f_R$ can be constructed to reduce and even remove the phase loss.

Notch filters are recommended in HDD literature over low pass filters for a sharper reduction in magnitude. The notch filters are low order and are easy to design and implement. A setback of these filters are that they are not robust to parameter variation. A resonant shift might cause instability of the closed-loop system.

4.3.2 VCM Controller

Many control strategies have been implemented and tested on dual-stage servo systems. Optimal LQG/LTR or post modern H_2/H_∞ controllers usually result in very high order controllers whose performance has little improvement over traditional ones. An effective and simple method discussed in [21] uses the practical PID-type lag-lead compensator. By tuning just one parameter, the controllers for both VCM loop and micro-actuator loop is designed at desired gain crossover frequency. In this dissertation, this method will be employed and illustrated below.

The VCM plant model will be that shown in equation (4.2). Suppose the VCM modes are compensated with notch filters described in the earlier section, the compensated plant model can be viewed as a double integrator at frequencies of interest:

$$G_V(s) = \frac{1.38 \times 10^8}{s^2} \tag{4.23}$$

then the VCM controller will be the following PID-type controller at desired gain crossover frequency f_V:

$$C_V(s) = K_V \frac{s + \frac{2\pi f_V}{2\alpha}}{s + 2\pi 10} \frac{s + \frac{2\pi f_V}{\alpha}}{s + 2\alpha 2\pi f_V} \tag{4.24}$$

$5 < \alpha < 10$ is recommended and is a parameter selected by the servo designer. After which K_V can be calculated by setting $|C_V(j2\pi f_V) G_V(j2\pi f_V)| = 1$.

In this example, $\alpha = 5$ and $f_V = 1000$ Hz. The compensated open loop transfer function has a -20 dB/dec slope during crossover and -40 dB/dec before and after crossover frequency of 1000 Hz. The lag-lead compensator converges to a standard Proportional-plus-Integral-plus-Derivative PID controller when the pole of the lag term approaches 0 and the pole of the lead term approaches ∞.

4.3.3 Micro-Actuator Controller

The PZT micro-actuator model will be that shown in equation (4.6). Suppose the PZT micro-actuator modes are compensated with notch filters described earlier,

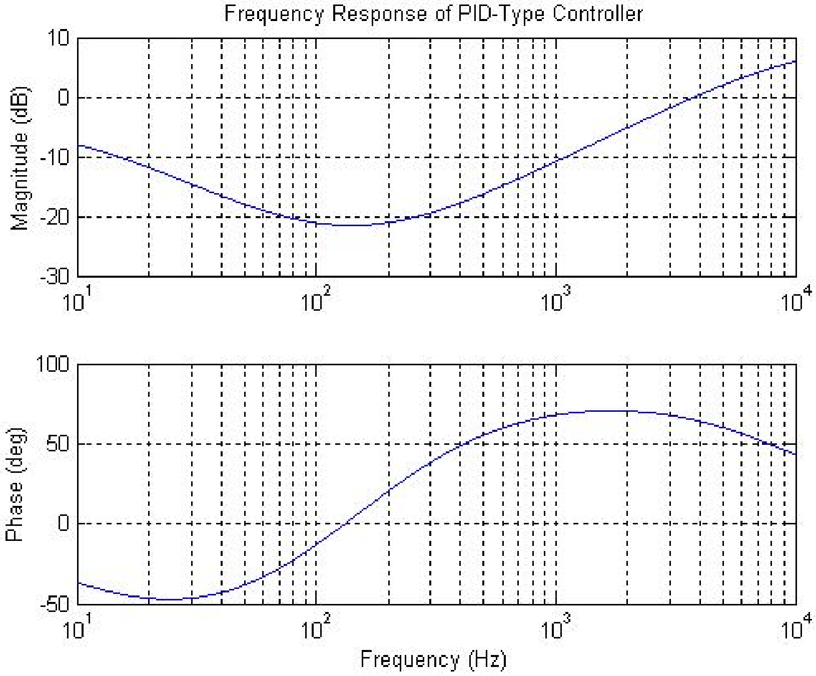

Figure 4.9: Frequency response of PID-type controller.

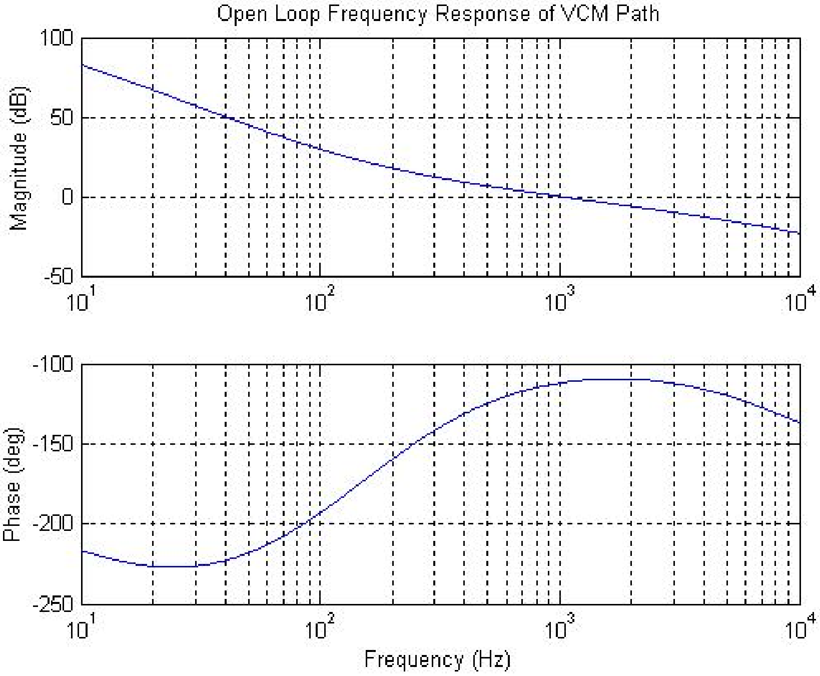

Figure 4.10: Open loop frequency response of VCM path.

the compensated plant model can be viewed as a pure gain at frequencies of interest:

$$G_M(s) = 0.282 \tag{4.25}$$

The secondary actuator path can then be stabilized by a simple PI-type lag compensator [21]:

$$C_M(s) = \frac{K_M}{s + 2\pi\frac{f_M}{g_M}} \tag{4.26}$$

where f_M is the gain crossover frequency for the micro-actuator path. g_M is a tuning parameter set by servo designer to avoid saturation of the micro-actuator path (usually low frequency gain of micro-actuator path). K_M can be found with the relation $|C_M(j2\pi f_M)G_M| = 1$.

In this example, $f_M = 3000$ Hz. The open loop transfer function has a -20 dB/dec slope during crossover. A DMS dual-stage control structure will be used.

4.3.4 Combined Results

The open loop frequency response is plotted in Figure 4.13. Figure 4.14 shows the sensitivity and complementary sensitivity function of the dual-stage servo loop. The step response of the combined actuation is shown in Figure 4.15. It should be noted that the secondary actuator actually reduces the overshoot of the system.

From Figures 4.13 and 4.15, it can be seen that the two actuators do not compete with each other during actuation which causes destructive interferences. At about 400 Hz, the phase difference between the VCM output and PZT micro-actuator output is about 90°.

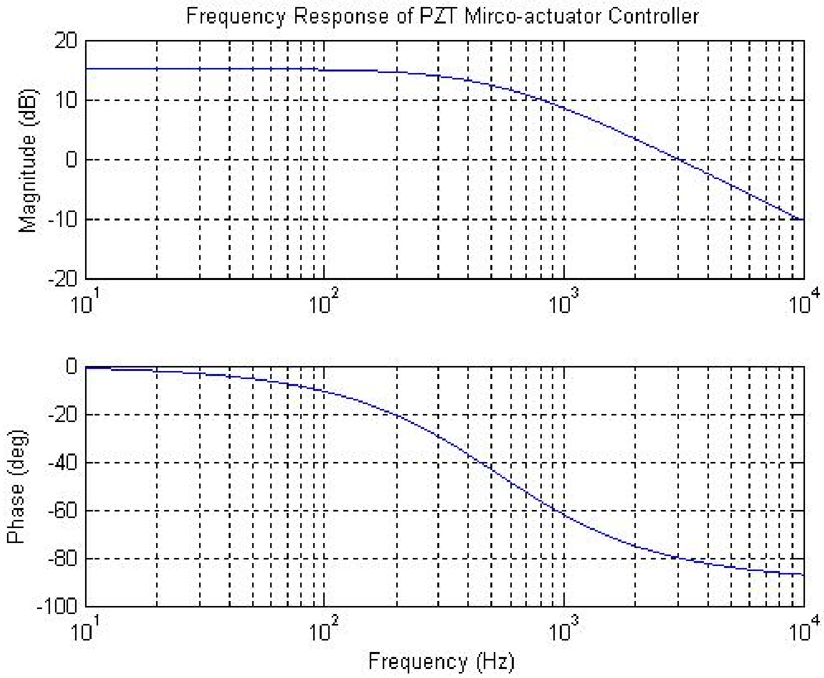

Figure 4.11: Frequency response of PZT micro-actuator controller.

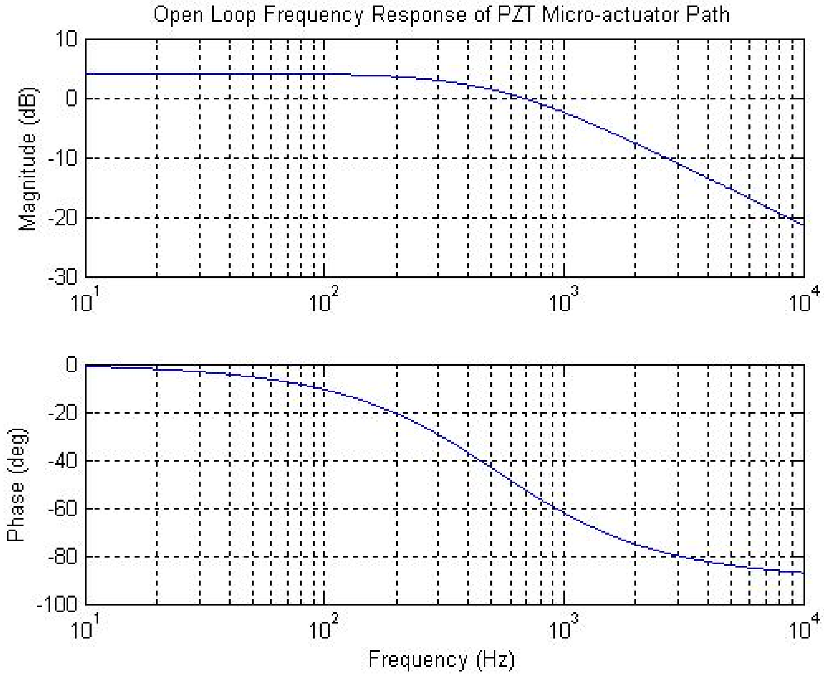

Figure 4.12: Open loop frequency response of PZT micro-actuator path.

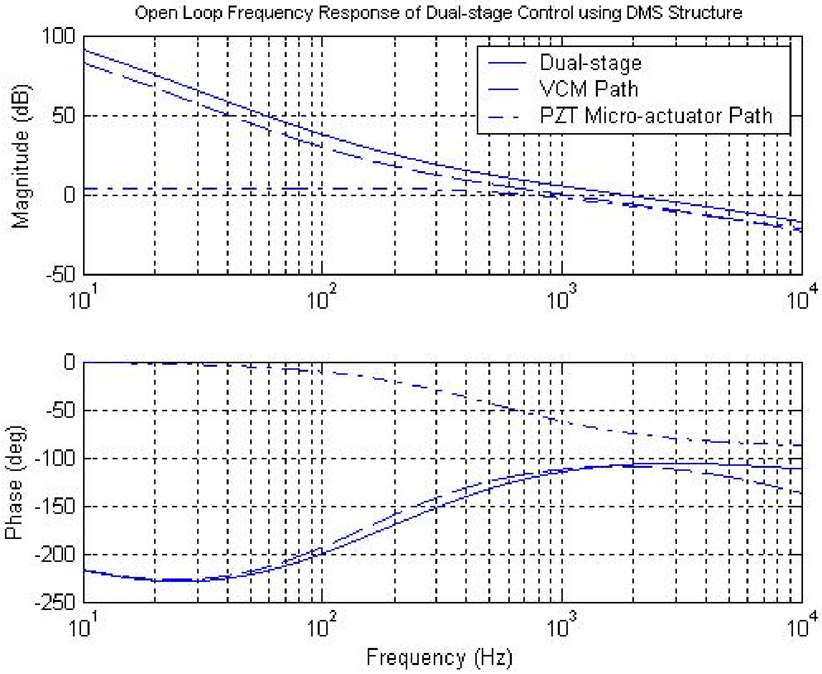

Figure 4.13: Open loop frequency response of dual-stage control using DMS structure.

Table 4.3: Design specifications achieved with dual-stage servo control

Open loop crossover frequency	$\approx$	2 kHz
Gain margin	$\geq$	20 dB
Phase margin	$\geq$	60°
Rise time	$<$	20 ms
Percentage overshoot	$<$	20%
Peak of sensitivity function	$\leq$	10 dB

It can be seen that the dual-stage servo system has a hump in the sensitivity function, which causes output disturbances (*eg.* disk platter vibrations) to be amplified in that frequency range. This is due to uncompensated anti-resonant

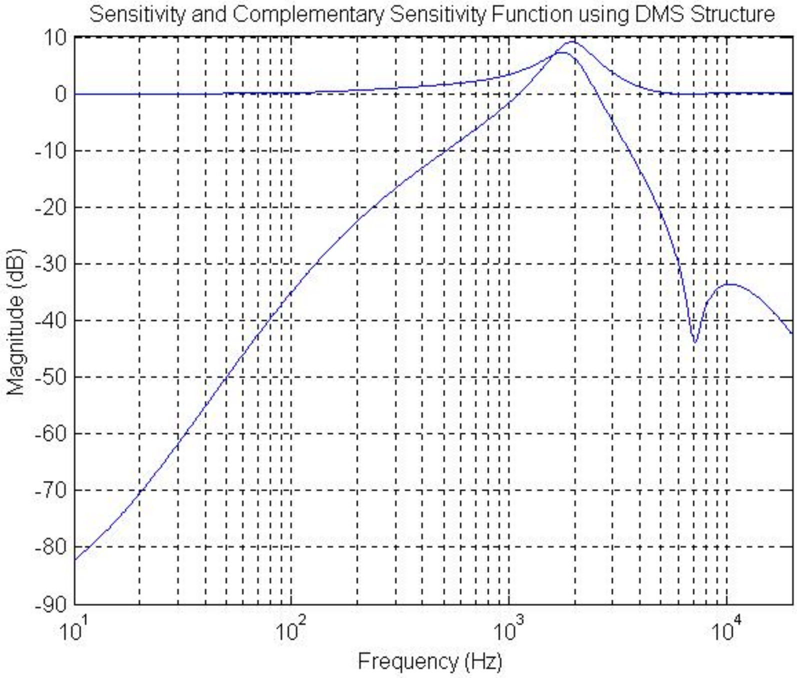

Figure 4.14: Sensitivity and complementary sensitivity function using DMS structure.

zeros which causes a low gain in the dual-stage open loop transfer function at high frequencies, resulting in the sensitivity function peaking above 0 dB. As such in order to enhance stronger disturbance rejection properties, it is desirable to model the PZT micro-actuator as a pure gain up to very high frequencies to avoid amplification of low and mid frequency band disturbances. This methodology includes compensation of both resonant poles and anti-resonant zeros and are covered in details in the next chapter.

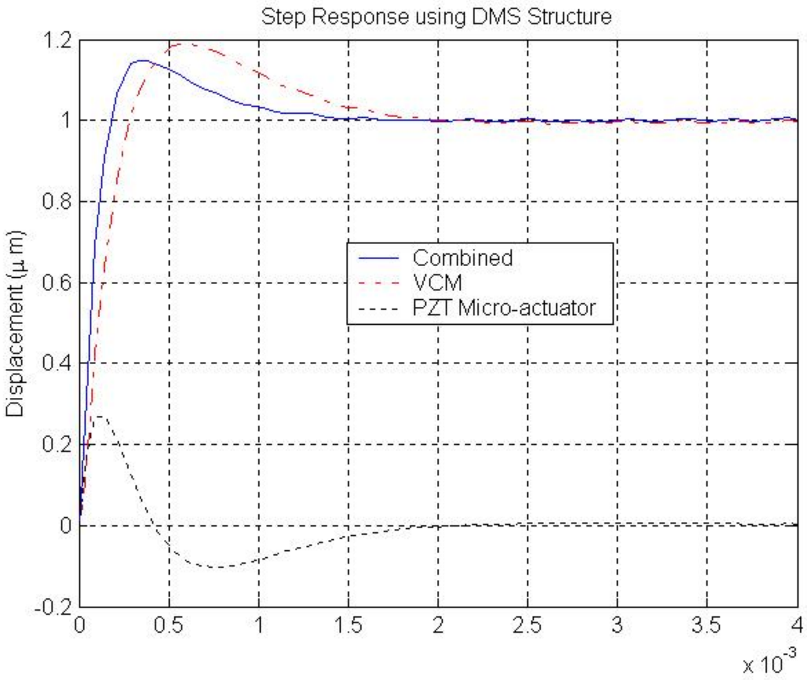

Figure 4.15: Step response using DMS structure.

4.4 Summary

In this chapter, the dynamics of the two actuators in a dual-stage HDD servo systems are discussed. From system identification to controller design, this chapter introduces the fundamentals of dual-stage control and common control topologies used. Notch filters are commonly used to suppress the actuators' mechanical structural resonances. After resonance compensation, a simple one parameter PID-type controller for both VCM and micro-actuator loop is presented. The effectiveness of these controllers are shown in the simulation results of the DMS dual-stage servo system.

The analysis in this chapter assumes continuous control of the HDD servo system. However due to discretization of the controllers and structural modes of the secondary actuator, much performance and disturbance rejection degradation will be expected. In the next chapter, we shall explore the feasibility of reducing the hump of the sensitivity function via loop shaping and proper modelling of the PZT micro-actuator to reduce system's relative degree.

Chapter 5

Suppressing Sensitivity Hump In Dual-Stage Servo Servo Systems

Next generation of high track density HDDs exert very stringent requirements on the servo positioning system. With the trend of higher recording densities and decreasing track pitch width, HDDs require excellent track-following performance and disturbance rejection capability. These qualities should be strengthened not only by increasing the open loop bandwidth but also reshaping the sensitivity frequency response.

However, the disturbance rejection capability of HDD servo loop is affected by both the servo bandwidth and the sensitivity hump. This chapter studies the sensitivity limitation in HDD dual-stage servo system and presents a control method to suppress the sensitivity hump to as low as possible. As such, high frequency disturbances would not be amplified by the servo loop and TMR would be reduced.

5.1 Background

HDD technology has been striving for larger data capacity and faster data transfer rate, which brings about the amazing increment of the track density and the disk spin speed. Currently, it is reported that the track density would exceed 150 kTPI (Tracks-Per-Inch) [63] and the disk spin speed would be 15000 rpm (revolution-per-minute) [24]. The narrower track width requires ultra-high positioning accuracy in HDD servo system. The faster disk revolution would cause much stronger air turbulence [22], which makes the positioning task even more challenging.

So far, the research in HDD servo has been focused on how to enlarge the servo bandwidth for the strong disturbance rejection capability [23]. The VCM in single stage servo system limits the bandwidth extension because of its resonances and uncertain modes [43]. The dual-stage servo system is proposed to place a secondary micro-actuator piggyback on the VCM. Because the micro-actuator has a much higher bandwidth than VCM, the servo bandwidth of dual-stage servo loop can be enlarged at least two times higher than single stage loop [33].

The disturbance within the servo bandwidth is suppressed by the servo loop, while the disturbance beyond the bandwidth could be amplified by the sensitivity hump. To minimize TMR, the height of sensitivity peak should be as low as possible. However in single stage servo system that uses VCM as the only actuator, the sensitivity hump appears unavoidable due to Bode's Integral Theorem (BIT) resulting in amplification of disturbances at high frequency band after gain crossover frequency. This implies a waterbed phenomenon in the sensitivity transfer function of servo loop *i.e.* more reduction at low frequency band would cause more amplification at high frequency band [16]. As such, extending the servo bandwidth to certain value would not decrease necessarily TMR.

Currently, the type of micro-actuators can be classified as three kinds according to the location [20]. They are the (i) suspension-based micro-actuator that is placed between the arm of VCM and the suspension (ii) slider-based micro-actuator that is inserted between the suspension and the slider and (iii) head-base micro-actuator that is attached between the slider and the read/write head. The suspension-based micro-actuator is often made of piezo-electric material, thus referred to as PZT micro-actuator. The other two kinds of micro-actuator are manufactured by the Micro-Electro-Mechanical-System (MEMS) technology hence MEMS micro-actuator.

In the following section, a dual-stage controller design procedure is presented for the PZT micro-actuator to reduce the peak of the sensitivity function of the dual-stage servo loop. It is shown that the sensitivity limitation from BIT is related to the relative degree of the micro-actuator model. The proper micro-actuator control design may suppress the sensitivity hump approaching 0 dB. Therefore, there is no trade-off of positioning accuracy between the extension of bandwidth and the amplification of disturbance.

5.2 Dual-Stage Controller Design

Much literature has been written on dual-stage control. In this chapter, the modified DMS dual-stage control structure with a non-linear estimator shown below in Figure 5.1 is used due to its simplicity and effectiveness in dealing with micro-actuator saturation [21].

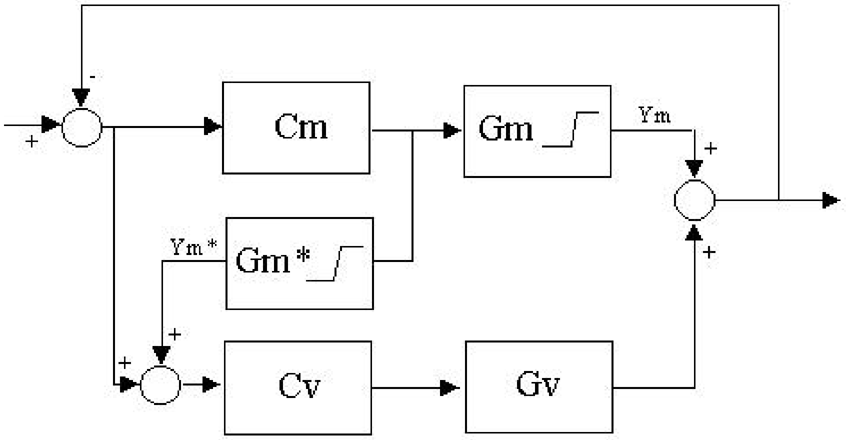

Figure 5.1: Modified decoupled master-slave configuration with non-linear estimator.

By employing the above, the sensitivities and control can be optimized separately for each loop. Now with S_V being the sensitivity function of the VCM loop and S_M as the sensitivity function of the micro-actuator loop, *i.e.*:

$$\begin{aligned} S_V &= \frac{1}{(1 + C_V G_V)} && (5.1) \\ S_M &= \frac{1}{(1 + C_M G_M)} && (5.2) \end{aligned}$$

Obviously $S_D = S_V S_M$. The Discrete Bode Integral Theorem described earlier in (2.7) can be rewritten as:

$$\int_{-\pi}^{\pi} \ln |S_D(e^{j\phi})| d\phi = \int_{-\pi}^{\pi} \ln |S_V(e^{j\phi})| d\phi + \int_{-\pi}^{\pi} \ln |S_M(e^{j\phi})| d\phi \qquad (5.3)$$

Because of the double-integrator properties of the VCM, the relative degree of the VCM discrete transfer function would be at least two. Hence $\int_{-\pi}^{\pi} \ln |S_V(e^{j\phi})| d\phi = 0$, which leaves us with

$$\int_{-\pi}^{\pi} \ln |S_D(e^{j\phi})| d\phi = \int_{-\pi}^{\pi} \ln |S_M(e^{j\phi})| d\phi \qquad (5.4)$$

implying that the area under the dual-stage sensitivity transfer function with such a structure is determined solely by the micro-actuator loop, as the attenuation by the micro-actuator path will remove the hump in the VCM path. The net area of S_D can be negative with proper modelling and control of the micro-actuator loop. There will be no disturbance amplification, with the possibility of even disturbance attenuation for many frequencies.

In the next subsection, the VCM controller is designed to satisfy the suggested shape of L possessing (i) high gain at low frequencies (ii) low gain at high frequencies and (iii) phase bounded away from ±180° to take advantage of feedback [55].

5.2.1 VCM Controller

Suppose the VCM resonant modes are compensated with notch filters described in previous chapter and the compensated model can be approximated by double-integrator at frequencies of interest. A PID type lag-lead compensator recommended in [21] will be used here again as the VCM controller. This simple and effective method presented requires the servo designer to tune only one parameter α with a desired gain crossover frequency f_V. A slight modification is made and the controller takes the following form:

$$C_V(s) = K_V \frac{s + \frac{2\pi f_V}{2\alpha}}{s + 2\pi 10} \frac{s + \frac{2\pi f_V}{\alpha}}{s + 2\alpha 2\pi f_V} \tag{5.5}$$

with $5 < \alpha < 10$ used typically. K_V can be calculated by setting $|C_V(j2\pi f_V)G_V(j2\pi f_V)| = 1$.

Due to the nature of the VCM's system order, the hump in S_V is unavoidable. The open loop transfer function of the VCM path L_V will enter SD as $\omega \to \infty$

for continuous time or $\phi \rightarrow f_s$ for discrete time systems. In the next subsection, we will make use of the secondary actuator loop to make the combined open loop transfer function L_D avoid SD or move along SD with little intersection.

Prior to micro-actuator controller design, we shall present a novel method of micro-actuator system identification. As mentioned earlier, a low order controller is desirable. A low relative degree micro-actuator controller will then be designed based on the identified model.

5.2.2 Near-Perfect Modelling (NPM)

The PZT micro-actuator can be described as a pure gain up to about $6 \sim 10$ kHz for the Φ-shaped actuated suspension [53] or even $10 \sim 30$ kHz for slider type actuator [37] where the first structural resonant mode occurs. The secondary actuator loop thus has a very high bandwidth and a large gain crossover frequency can be assigned. This high bandwidth property of the PZT micro-actuator allows better disturbance rejection at the frequencies the VCM could not achieve alone.

Using the fact that $S_D = S_V S_M$ in DMS structure, the hump in S_V can be cancelled by S_M as $|S_M| < 1$ for those frequencies. On higher frequencies, care must be taken to control the PZT micro-actuator so that there is no hump in S_M. Conventional notched-base servo which compensates for the resonant poles in the PZT micro-actuator alone is insufficient as the loop gain $|C_M G_M|$ at the frequencies of the anti-resonant zeros are very small, and hence causing a hump in the sensitivity function at these frequencies which can be seen from the relation $S_M = \frac{1}{1+C_M G_M}$. As such, the anti-resonant zeros should be compensated as well to achieve a low hump for better disturbance rejection. This can be done if the PZT micro-actuator behaves as a pure gain up to high frequencies and a low relative degree controller is used, and can be seen via inspection of equation (5.4). The frequency response of a PZT micro-actuator shown below is identical to that in Figure 4.4.

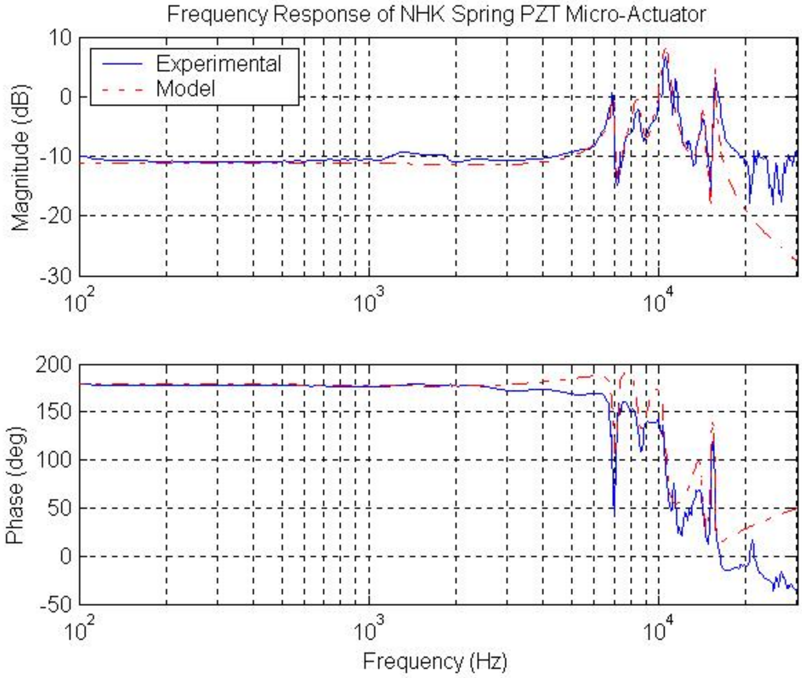

Figure 5.2: Frequency response of PZT micro-actuator.

By modelling the PZT micro-actuator as a pure gain up to higher frequencies, the above ideal qualities can be achieved. This pure gain modelling involves pre-multiplying the PZT micro-actuator with a model inverse to make the compensated PZT micro-actuator behave as a unity gain system with zero phase for frequencies up to about 10 kHz. Higher frequencies cannot be achieved due to low-pass nature of the plant (plant model when inverted gives improper transfer function) and high frequency plant uncertainties. The model inverse not only compensates for the resonant modes of the secondary actuator but also cancels the stable anti-resonant zeros. We shall termed this method as "Near-Perfect Modelling" (NPM).

NPM method seeks for resonant pole and anti-resonant zero pairs up to frequency of interest, noting that each pair gives a second-order transfer function. NPM is applicable only to the PZT micro-actuator loop and not the VCM loop as the PZT micro-actuator model inverse is proper while the VCM model inverse is improper. For better results, NPM constructs the model inverse via ZOH (Zero-Order Hold) method. If any poles or zeros in particular are outside the unit disc after discretization, they are discretized using pole-zero matching with frequency pre-warping instead. The experimental compensated frequency response of the PZT micro-actuator after NPM is shown in Figure 5.3.

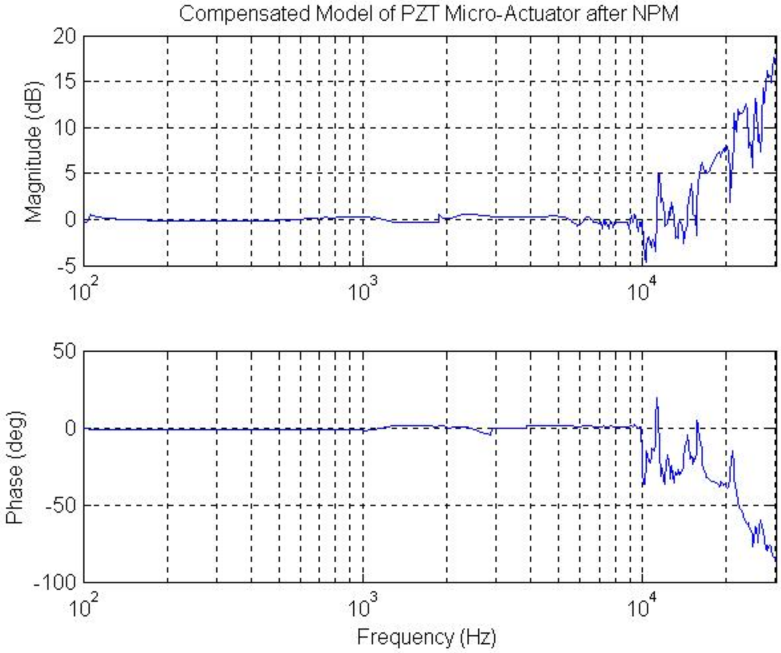

Figure 5.3: Compensated frequency response of PZT micro-actuator after NPM.

It should be noted that the high gain at frequencies after NPM is intended. This high gain occurs in high frequencies compared to the closed-loop bandwidth of the PZT micro-actuator path and hence closed-loop stability will not be affected. The high gain at high frequencies causes the open loop transfer function L_D to avoid SD as $\omega \rightarrow \infty$ or $\phi \rightarrow f_s$. This causes better error rejection even at high frequencies.

5.2.3 PZT Micro-Actuator Controller

The PZT micro-actuator can be viewed as a pure unity gain up to very high frequencies after pre-multiplying with model inverse from NPM. With this, we shall discuss in the following subsections two control strategies used and their capabilities in disturbance rejection. The usage of a first order pure lag compensator (a lag compensator without any zero) and that of a first order lag compensator (a lag compensator with a pole and zero) for C_M will be compared. To differentiate between the two lag compensators, the first order pure lag compensator will be called a Proportional-plus-Integral (PI) type controller for simplicity but without loss of generality.

PI-Type Control

Suppose the PZT micro-actuator resonant modes and anti-resonant zeros are compensated with model inverse from NPM. The simple yet effective first order pure lag compensator described in [21] is employed here. Similar to the VCM controller, the PZT micro-actuator path controller only has one parameter g_M to be tuned by the servo designer:

$$C_M(s) = \frac{K_M}{s + 2\pi \frac{f_M}{g_M}} \tag{5.6}$$

where f_M is the gain crossover frequency for the PZT micro-actuator path. g_M is a tuning parameter chosen to avoid saturation of the micro-actuator path (usually low frequency gain of the PZT micro-actuator path). K_M can be found with the relation $|C_M(j2\pi f_M)G_M(j2\pi f_M)| = 1$.

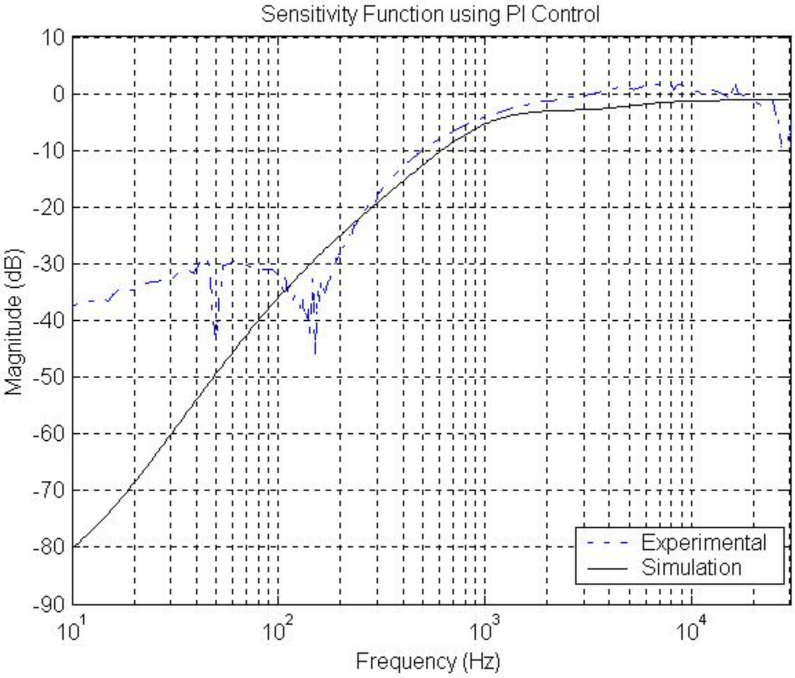

Figure 5.4: Sensitivity function using PI control.

The simulation and experimental results agree closely. This shows that NPM offers a good fit and disturbance rejection capabilities are enhanced. The experiment $||S||_\infty$ is about 2 dB. The ideal peak value from simulation is hard to attain due to modelling uncertainties and unintentional phase loss. The intended error rejection at high frequencies is obtained. The experimental step response of 0.3 μm, VCM control signal and PZT micro-actuator control signal are shown in Figure 5.5, Figure 5.6 and Figure 5.7 respectively.

In the next subsection, the peak of S_D is further reduced using DBIT.

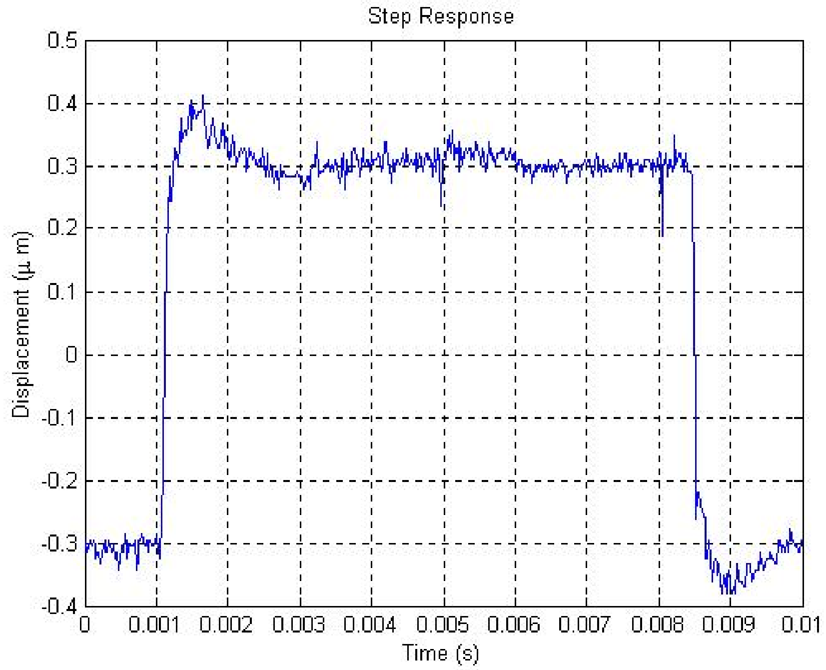

Figure 5.5: Step response.

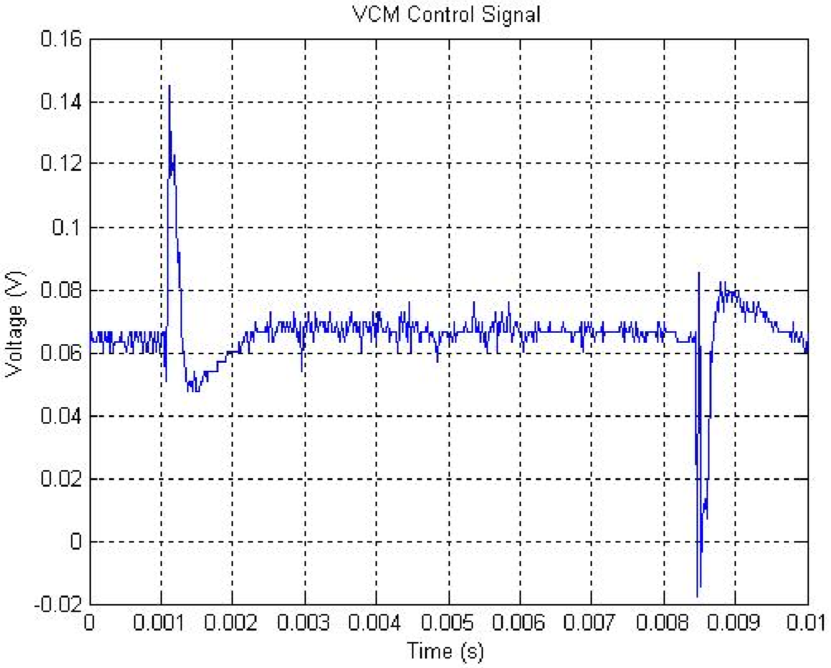

Figure 5.6: VCM control signal.

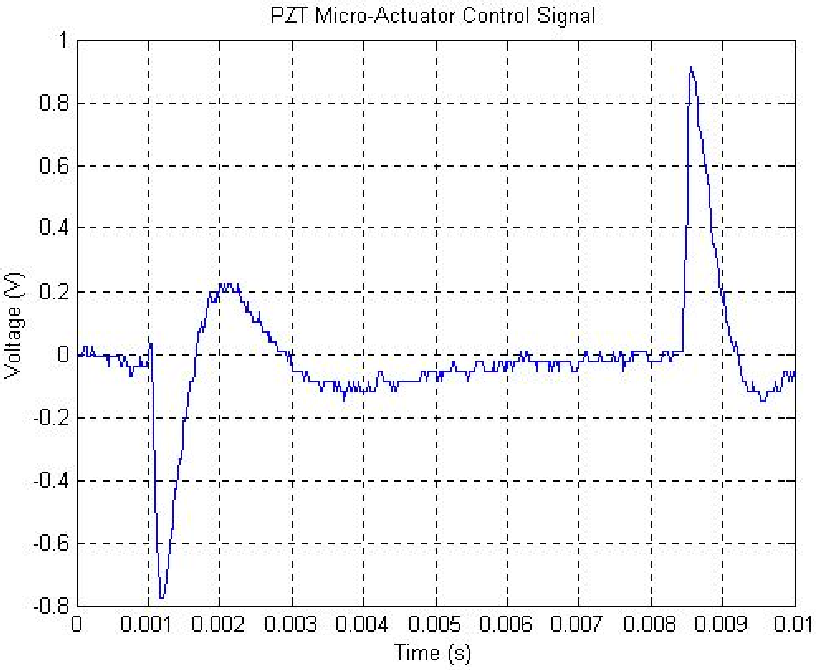

Figure 5.7: PZT micro-actuator control signal.

First Order Lag

In this subsection, a first order lag compensator is used instead. A modification to the PI controller mentioned in previous subsection takes the form:

$$C_M(s) = K_M \frac{s + \frac{2\pi f_s}{\beta}}{s + 2\pi \frac{f_M}{g_M}} \tag{5.7}$$

where f_M and g_M are same as above. f_s is the Nyquist frequency and β is a tuning parameter for intended disturbance attenuation. $1 < \beta \leq 3$ is used typically, and K_M can be found with the relation $|C_M(j2\pi f_M)G_M(j2\pi f_M)| = 1$.

The main motivation of adding an additional zero to C_M is to enhance phase lifting of L_D and at the same time retain the low gain after gain crossover frequency for stability. This also reduces the relative degree of the PZT micro-actuator path. The idea is apparent from the Nyquist plot of L_D. By adding a simple zero, L_D

will approach SD with the conditions satisfied mentioned earlier *i.e.* avoid SD and approach the origin at $-\frac{\pi}{2} \leq \angle L(j\omega) \leq \frac{\pi}{2}$.

Now let $C_V G_V = \frac{N_V^{[A]}}{D_V^{[B]}}$. N_V and D_V are the numerator and denominator of the open loop VCM path with $[A]$ and $[B]$ being the orders of the associated transfer function polynomial. Similarly, let $C_M G_M = \frac{N_M^{[C]}}{D_M^{[D]}}$. N_M and D_M will be the numerator and denominator of the open loop PZT micro-actuator path with $[C]$ and $[D]$ being the orders of the associated transfer function polynomial. The differences $B - A$ and $D - C$ are relative degrees of the VCM path and PZT micro-actuator path respectively. For the VCM path, $B - A \geq 2$ due to its double integrator properties.

In a DMS configuration, the overall open loop transfer function in (4.19) can re-expressed using the above:

$$\begin{aligned} L_D &= (1 + C_M G_M) C_V G_V + C_M G_M \\ &= (1 + \frac{N_M^{[C]}}{D_M^{[D]}}) \frac{N_V^{[A]}}{D_V^{[B]}} + \frac{N_M^{[C]}}{D_M^{[D]}} \\ &= \frac{N_V^{[A]} D_M^{[D]} + N_V^{[A]} N_M^{[C]} + D_V^{[B]} N_M^{[C]}}{D_V^{[B]} D_M^{[D]}} \end{aligned} \tag{5.8}$$

After NPM, the relative degree of the compensated PZT micro-actuator path is zero for many frequencies. By adding a high frequency zero to C_M, $D - C = 0$ for many frequencies compared to $D - C = 1$ using PI control. Now let N_D and D_D be the numerator and denominator of the dual-stage open loop, we get from equation (5.8):

$$L_D = \frac{N_D^{[B+C]}}{D_D^{[B+D]}} = \frac{N_D^{[B+D]}}{D_D^{[B+D]}} \tag{5.9}$$

It can be seen from equation (5.9) that the addition of $C_M G_M$ actually reduces the relative degree of the dual-stage open loop transfer function to zero even though the relative degree of the open loop VCM path in single stage configuration is at least two! The PZT micro-actuator employed in dual-stage control not only decreases sensitivity by increasing the bandwidth but is also able to reduce system's relative order for disturbance suppression when employed properly. The addition of the high frequency zero hence forces L_D out of SD into the open right half complex plane, satisfying the conditions for design earlier as can be seen in Figure 5.8. Conventional notch-based servo causes the open loop transfer function of dual-stage servo to “remain” in SD for many frequencies while the phase-stabilized servo method describe by authors in [32] results in big loop circles and the open loop transfer function enters and leaves SD many times especially at resonant frequencies. This simple method of NPM and first order lag described offers little intersection with SD. NPM methodology offers a low hump using PI control, and can even be suppressed further with a first order lag. NPM method also provides good phase and gain margins.

The sensitivity function using a first order lag is shown below in Figure 5.9. A low relative degree PZT micro-actuator controller after NPM offers not only disturbance suppression but even attenuation.

The feasible solution for open loop shape in [55] used in PI control is compared with that using the first order lag. Instead of a low gain at high frequencies, the placement of a high frequency zero causes a fairly constant small gain at high frequencies. The open loop transfer function for both methods are shown in Figure 5.10.

With $S + T \equiv 1$, the trade-off between desirable small S and small T simultaneously is unavoidable. As such, the main setback of such a method is that the high

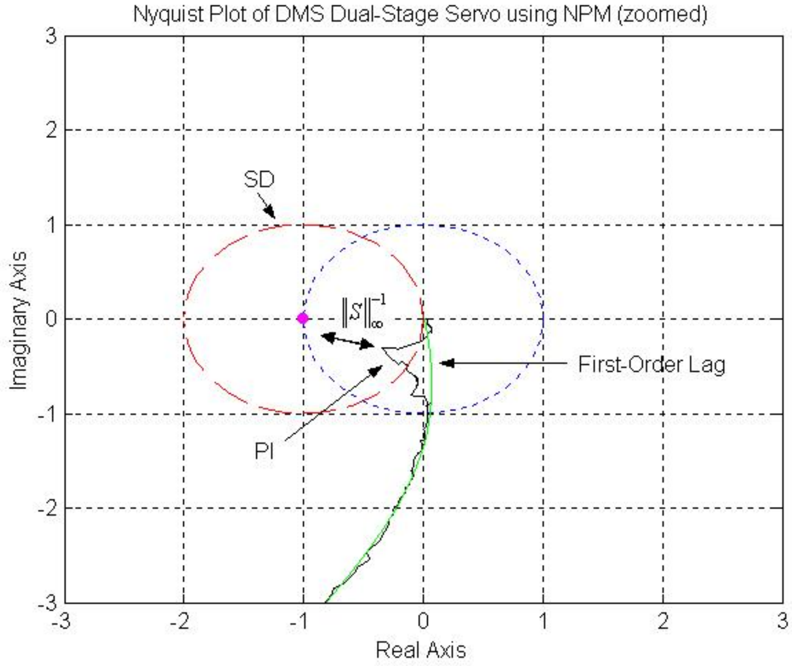

Figure 5.8: Nyquist plot of dual-stage servo using NPM (zoomed).

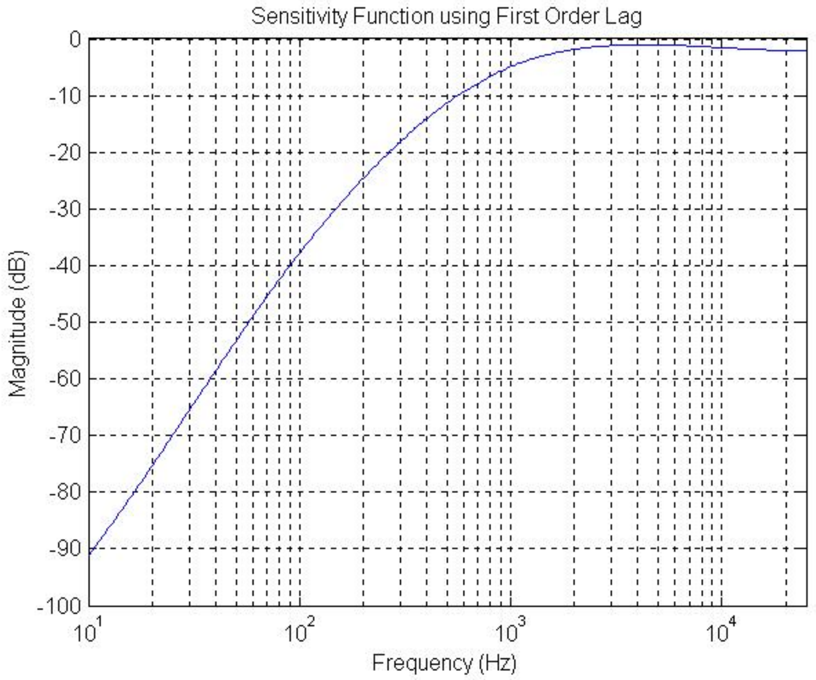

Figure 5.9: Sensitivity function using first order lag.

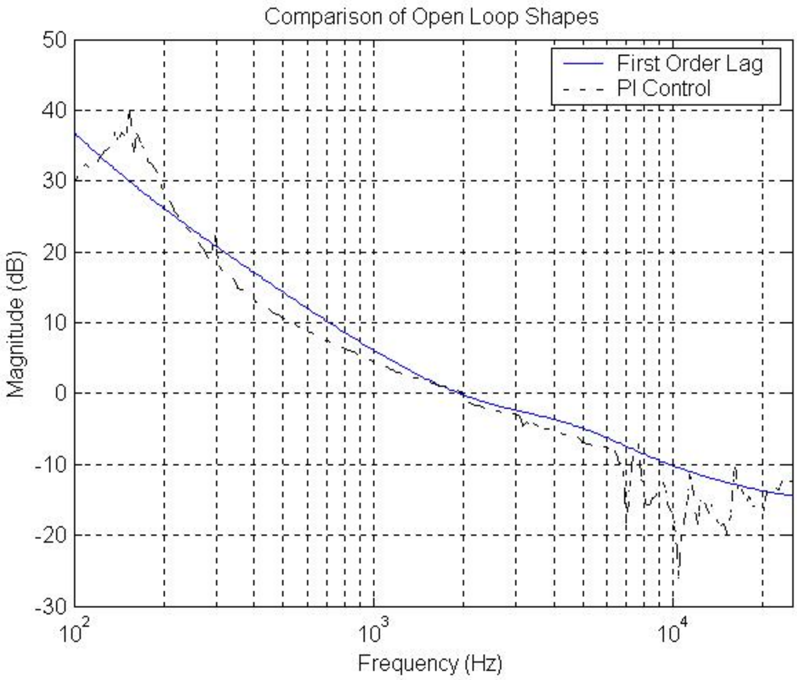

Figure 5.10: Comparison of open loop shapes.

frequency roll-off of the system will be compromised as can be seen in Figure 5.11 below. This is usually intolerable as measurement noise in the PES demodulation channel and plant high frequency uncertainties will not be attenuated. However, the low pass nature of the physical systems will take care of these constraints at higher frequencies. In the next section, the performance of such a design will be evaluated via simulations.

5.3 Performance Analysis

To illustrate the effectiveness of the designed dual-stage servo system and the implications of less high frequency roll-off, the effects impulse torque disturbances and PES measurement noise will be simulated.

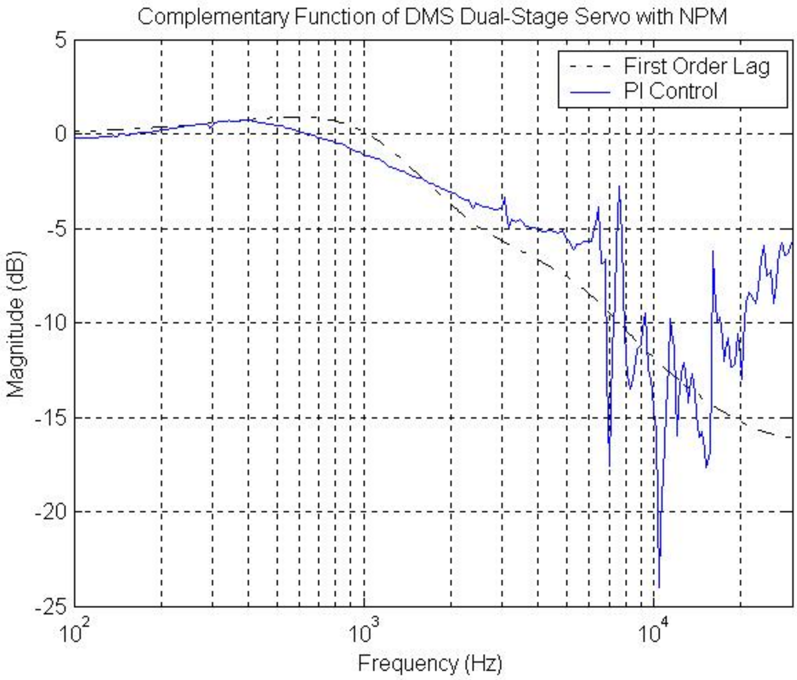

Figure 5.11: Comparison of complementary sensitivity function.

5.3.1 Impulse Torque Response

An example of impulse torque disturbances affecting the servo positioning accuracy is the residual vibration response at the end of track seeking. The actuators then change into track settling mode, and notch-based servo which works effectively only for steady-state operations cannot reduce the vibrations cause by the large initial states of the actuators. As such, it would be important to analyze the effects of impulse torque disturbances on the head/slider off-track.

Compared to notch-based and phase-stabilized servo in [32] which takes about 5 ms for the disturbances of relatively large amplitudes to be rejected, the designed dual-stage servo can compensate for the residual vibrations in less than 1 ms.

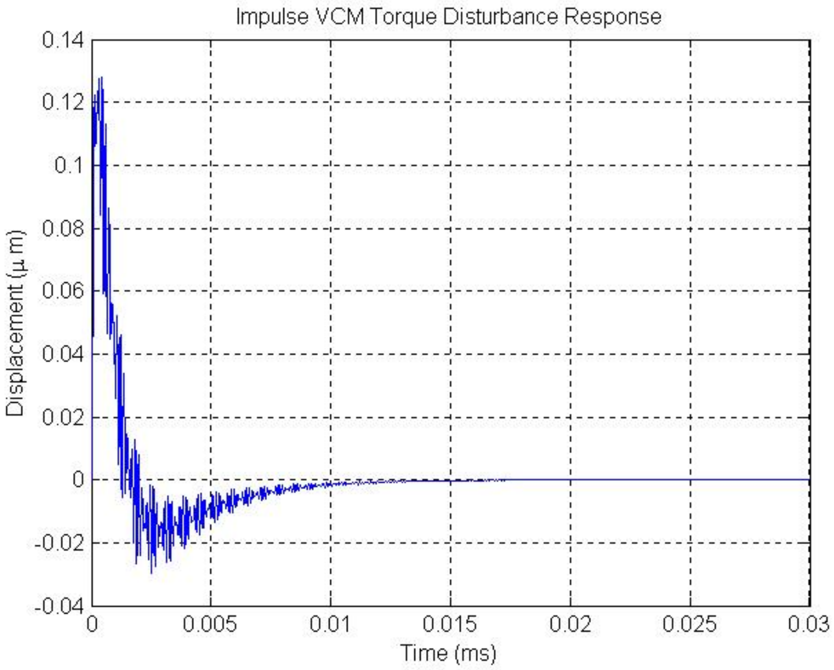

Figure 5.12: Impulse VCM torque disturbance response.

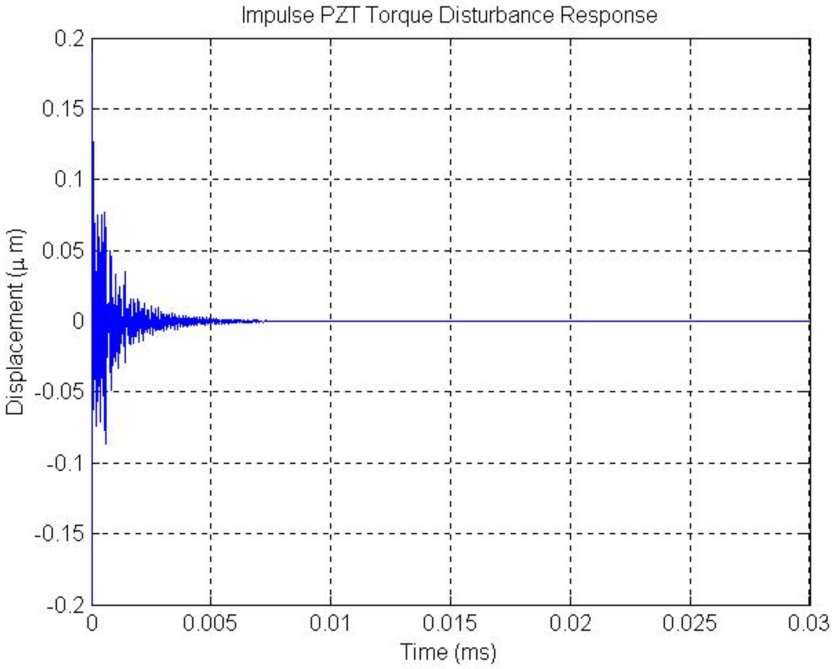

Figure 5.13: Impulse PZT micro-actuator torque disturbance response.

5.3.2 Noise Response

As mentioned in previous sections, the high frequency roll-off of the designed dual-stage open loop transfer function is reduced to enable better disturbance capabilities. This in fact would compromise the noise and uncertainties attenuation capabilities at high frequencies. To study the effects of measurement noise on true PES, a noise model created by authors in [11] is added into the servo loop to simulate PES measurement noise.

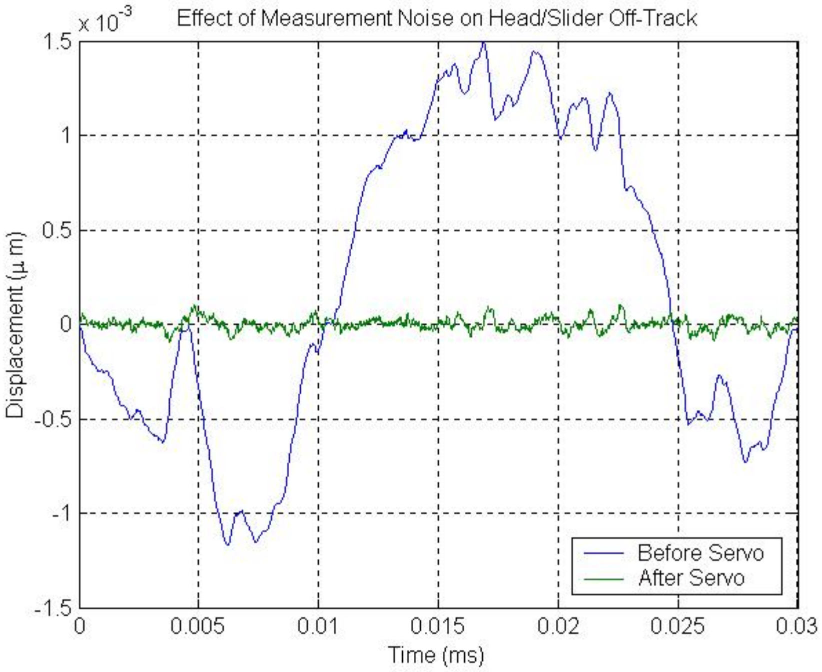

Figure 5.14: Effect of measurement noise on head/slider off-track.

It can bee seen from Figure 5.14 that much of the measurement noise contaminating the true PES is still effectively removed. In the next section, the other issue of less high frequency roll-off of the designed open loop transfer function *i.e.* plant model uncertainties will be addressed.

5.3.3 Sensitivity Robustness

The dual-stage servo is designed based on mathematical models identified from an operating range of frequencies of the actuators. This approximation of true dynamics of the actual plant and model used results in modelling uncertainties. Plant uncertainties on the other hand arises from plant parameter perturbations under various operating conditions and manufacturing environments. In this section, the sensitivity robustness of the designed dual-stage servo will be analyzed with effects of ±5 % resonant frequency shifts in the PZT micro-actuator, as can be seen in Figure 5.15.

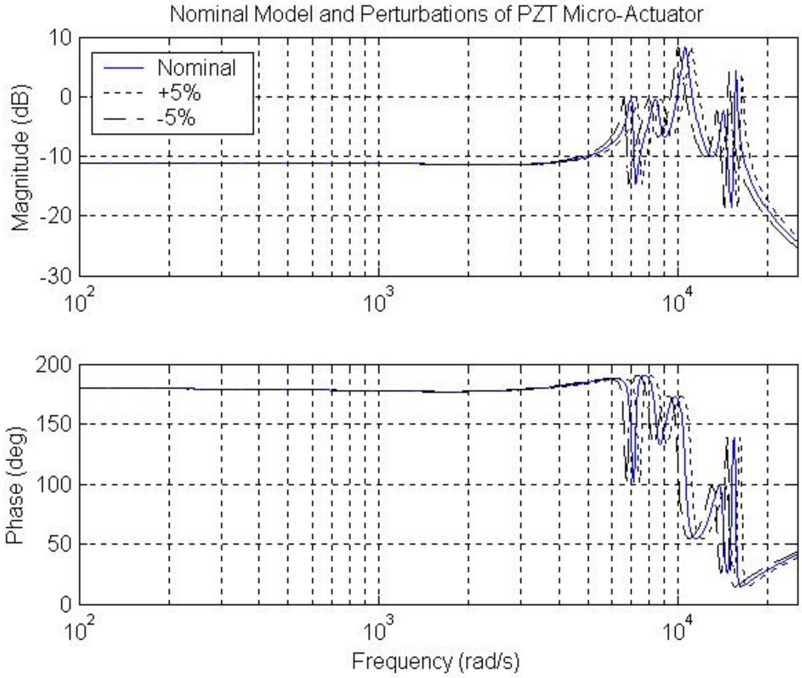

Figure 5.15: Nominal model and ±5 % resonant frequency perturbations of the PZT micro-actuator.

Although NPM methodology seems not robust to parametric perturbations and other uncertainties, the dual-stage closed-loop system is still stable under the resonant frequency shifts. Disturbance rejection capabilities are still retained as shown in Figure 5.16 below. The shifts in resonant frequencies cause slight pole-zero mismatch, but the peaks of the humps are still very small and spread over a large frequency range.

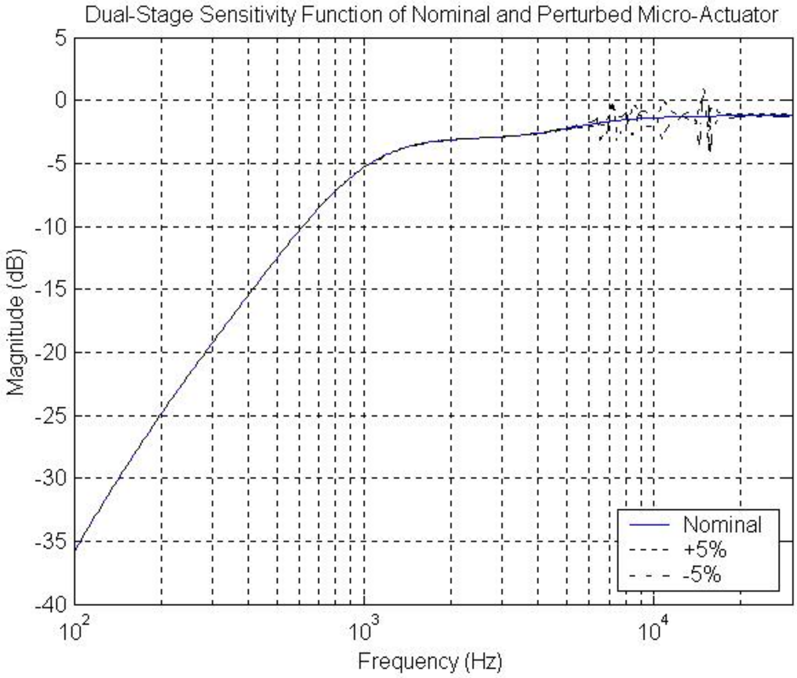

Figure 5.16: Sensitivity of nominal and perturbed PZT micro-actuator.

5.3.4 Effect of Sampling Rate

In continuous time, BIT and waterbed effect occurs over the entire frequency spectrum. However in sampled-data system of HDDs, the waterbed effect must be "completed" before the Nyquist frequency [2]. A high sampling rate is hence desirable to "stretch" the frequency range and spread the positive area (hump) under $S(e^{j\phi})$ over a larger frequency range to reduce the peak. This would effectively prevent amplification of disturbances in the low frequency band, at the expense of more PES noise and uncertainties in the higher frequency band. This usage of computational power for disturbance rejection shall be further explored in this section.

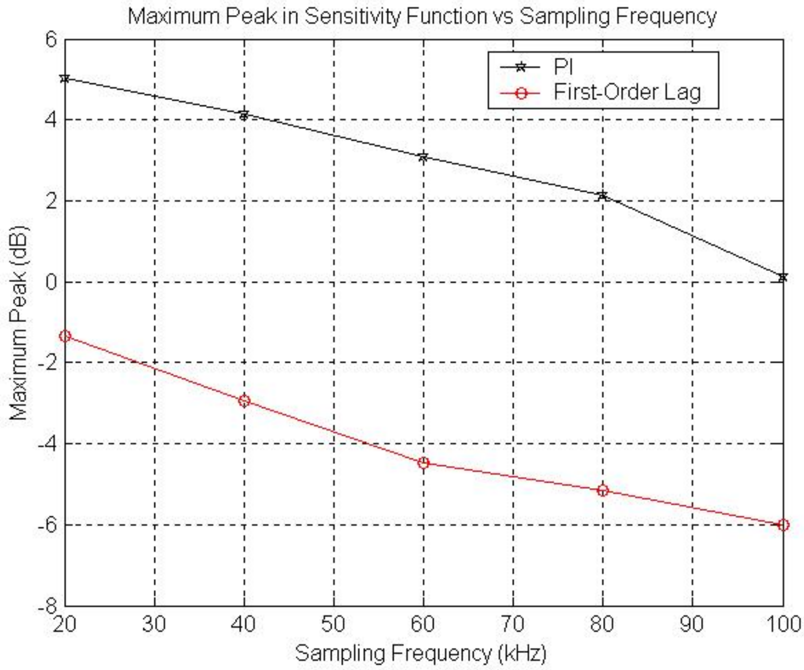

Figure 5.17: Graph of $||S||_\infty$ (dB) vs sampling rate.

Repeating the simulation and experiment using the controllers mentioned in earlier sections at different sampling frequencies, the corresponding $||S||_\infty$ can be graphed in Figure 5.17. As expected, increasing sampling frequency is indeed a feasible option when better disturbance rejection capabilities are needed. Although increasing number of servo sectors for implementing high sampling rate is one of the solutions, user data storage capacity will be compromised as a result. An approach of high sampling frequency can be achieved via extracting position information from user data as well [56].

5.4 Conclusion

In this chapter, a feasible way to relax the waterbed effect on the dual-stage servo system in HDDs is explored. It is shown that the relative degree of the micro-actuator path is the key to bypass the waterbed effect in the dual-stage servo loop. For better disturbance rejection (even attenuation) capabilities, NPM modelling and a low relative degree micro-actuator controller are proposed to achieve a sensitivity hump approaching 0 dB. The effectiveness of the design methods and high sampling frequency are demonstrated by experimental results. Design considerations and guidelines are also be presented in the chapter. TMR in track-following would be reduced not only by higher servo bandwidth but also less amplification, even attenuation of high frequency disturbances.

Chapter 6

Conclusion and Future Work

The trend of increasing storage density for higher TPI demands good disturbance rejection capabilities in HDD servo control systems. This dissertation focuses on studying disk platter vibration behaviors and solutions using high performance positioning mechanism of dual-stage actuation system for disturbance suppression and attenuation.

The main findings and results presented in this dissertation are :

1. The mode shapes of a disk are captured and the natural frequencies, vibration amplitudes (and phases) on higher rotational speeds are projected based on an experimental approach. A RLS algorithm is used to regress the natural frequencies and vibration amplitudes on rotating speed. This approach allows the amplitude, mode shape and natural frequency of disk platter vibration to be known on rotation speed in rpm. The effect of disk-spindle imbalance is also briefly discussed.

2. A time domain disk vibration disturbance model is constructed based on the identification results. The simulation block diagram developed is used to convert axial vibration to slider off-track, enabling a better design for track following controller. With the amplitude, frequency and mode shape of vibration, designing a closed-loop servo system with a pre-determined rotation speed in rpm to avoid amplification of disk flutter vibrations at the peaking of the sensitivity transfer function can be achieved. Feedforward disk vibration compensation can also be easily designed off-line.

3. A sensitivity analysis (with design considerations) is performed on the servo control loop and the Bode's Integral constraints on the dual-stage servo system are studied. It is concluded that a low relative degree micro-actuator path in a DMS control structure is essential to bypass the "waterbed" effect and suppress the sensitivity hump in dual-stage servo systems.

4. For better disturbance rejection (even attenuation) capabilities, NPM modelling and a zero relative degree, first-order micro-actuator controller are proposed to achieve a low sensitivity hump. The effectiveness of the proposed design methods are verified with experimental results. The effects of different sampling rates for disturbance rejection is also studied. Design guidelines and considerations for low sensitivity hump are presented.

Mechanical vibrations limit achievable TPI and will continue to be so. Excellent disturbance rejection capabilities for HDD servo system will hence be essential. In view of the results obtained, the following work should be emphasized in future research :

1. Order analysis of disk platter vibrations :

Order analysis involves extracting sinusoidal components of vibration signals as harmonic orders of rpm under periodic loading [18]. Instead of using the waterfall plot (or Cambell diagram) to study disk platter resonances and vibrations, order analysis can be used for rotating disks. Order analysis enable the rotational and structural disk platter vibrations to be separated accurately. Critical rotation speeds and natural frequencies can then be identified easily.

2. Vold-Kalman Filtering of disk vibration signals :

   Disk platter vibrations are usually modelled and analyzed in the frequency domain off-line. The advantage of using Vold-Kalman Filtering is that disk platter vibration signals in time domain can be used for mode and order analysis. The PAS will be easily obtained and hence possible online feedforward compensation can be employed [18].

3. Application of dual-stage control to Servo Track Writing (STW) technology :

   Dual-stage actuation is currently studied on HDD servo systems for track following or short span seek only. With the high bandwidth and good disturbance rejection capabilities offered by dual-stage actuation, this technology can be introduced to STW technology for higher TPI demonstration. The RRO components in PES can be removed at the source during the servo track writing process. The NPM and control methods presented in Chapter 5 can be used for better disturbance rejection in the STW control loop.

4. Robust and optimal control methods for dual-stage actuation :

   Control optimization with robust objectives and better disturbance rejection will continue to be a challenge and important to the HDD industry. The feasibility of solving the concave optimization problem with mixed H_2/H_∞ objectives including robust considerations on S, T and KS can be further explored. A proposed feasible cost function to reduce the quadratic H_2 cost :

$$J_2 = \left\| \begin{matrix} W_S^2 S \\ W_T^2 T \\ W_u^2 KS \end{matrix} \right\|_2^2$$

subjected H_∞ bound of :

$$\left\| \begin{matrix} W_S^\infty S \\ W_T^\infty T \\ W_u^\infty KS \end{matrix} \right\|_\infty \leq \gamma$$

where W_S, W_T and W_u are the weighting filters which give appropriate weight to the transfer functions S, T and KS respectively.

Bibliography

[1] D. Abramovitch and G. Franklin, “A Brief History of Disk Drive Control,” *IEEE Control Systems Magazine*, June 2002.

[2] D. Abramovitch, T. Hurst and D. Henze, “The PES Pareto Method : Uncovering the Strata of Position Error Signals in Disk Drives,” *Proc. American Control Conference*, pp. 421–428, Albuquerque, NM, June 1997.

[3] K. J. Astrom and B. Wittenmark, *Computer Controlled Systems : Theory and Design*, Prentice Hall, 3^{rd} edition, 1997.

[4] G. Bouchard and F. E. Talke, “Non-Repeatable Flutter of Magnetic Recording Disks,” *IEEE Trans. on Magn.*, Vol. 22, No. 5, September 1986.

[5] Y. Chang, D. Park, N. Park and Y. Park, “Prediction of Track Misregistration Due to Disk Flutter in Hard Disk Drive,” *IEEE Trans. on Magn.*, Vol. 38, No. 2, March 2002.

[6] B. M. Chen, *Robust and H_∞ Control*, Springer-Verlag, New York, London, 2000 (Communications and Control Engineering Series).

[7] B. M. Chen, T. H. Lee and V. Venkataramanan, *Hard Disk Drive Servo Systems*, Springer-Verlag, New York, London, 2002 (Advances in Industrial Control Series).

[8] R. Chen, "Advance Control Designs for Hard Disk Drive Servo Systems," *PhD Thesis*, National University of Singapore, 2001.

[9] R. Chen, G. Guo and T. S. Low, "An Intersample Ripple Free Multirate Servo Controller for Disk Drive Actuators," *Proc. 25th IECON*, pp.1171–1176, 1999.

[10] J. C. Doyle, B. A. Francis and A. R. Tannenbaum, *Feedback Control Theory*, Macmillan, 1992.

[11] C. Du, J. Zhang and G. Guo, "Vibration Analysis and Control Design Comparison of Fluid Bearing and Ball Bearing HDDs," *Proc. of American Control Conference*, pp. 1380–1385, Anchorage, AK, May 8-10, 2002.

[12] R. Evans, J. Griesbach and W. Messner, "Piezoelectric Micro-Actuator for Dual-Stage Control," *IEEE Trans. Magn.*, Vol. 35. No. 2, pp. 977–982, March 1999.

[13] G. Ferretti, A. Furlan, G. Magnani, G. Maiocchi and P. Rocco, "Dynamic Model of a Multiple Disk and Spindle Assembly," *2001 IEEE/ASME International Conference on Advanced Intelligent Mechatronics Proceedings*, Como, Italy, 8-12 July 2001.

[14] G. F. Franklin, J. D. Powell and M. Workman, *Digital Control of Dynamic Systems*, Addison-Weasley, 3^{rd} edition, 1997.

[15] J. Freudenberg, R. Middleton and A. Stefanopoulou, "A Survey of Inherent Design Limitations," *Proc. American Control Conference*, pp. 2987–3001, Chicago, Illinois, USA, June 2000.

[16] H. Fujita, K. Suzuki, M. Ataka and S. Nakamura, "A Microactuator for Head positioning System of Hard Disk Drives," *IEEE Trans. on Magn.*, Vol. 35, No. 2, pp. 1006–1010, March 1999.

[17] Fujitsu Company Website [Online], Fujitsu develops HDD Read-Head Technology for 300 Gb/in^2 Densities, *http://pr.fujitsu.com/en/news/2002/05/15-1.htm*, May 2002.

[18] S. Gade, "Advance Sound and Vibration Measurements & Applications Seminar," conducted by Brüel and Kjær (South Asia Pacific) Pte Ltd, Singapore, 14th January 2003.

[19] L. Guo and Y. D. Chen, "Disk Flutter and Its Impact on HDD Servo Performance," *IEEE Trans. on Magn.*, Vol. 37, No. 2, March 2001.

[20] L. Guo, D. Martin and D. Brunnett, "Dual-Stage Actuator Servo Control for High Density Disk Drives," *Proc. 12th IEEE Int. Conf. on Advanced Intelligent Mechatronics*, pp. 132–137, Atlanta, Usa, September 1999.

[21] G. Guo, D. Wu and T. C. Chong, "Nonlinear Dual-Stage Control Design Considering Micro-Actuator Saturation," *Pre-print of IFAC Mechatronic Conference*, 2002.

[22] G. Guo and J. Zhang, "Active Control for Reducing Disk Flutter Induced Track Mis-Registration," *Digest of Asia-Pacific Magnetic Recording Conference 2002*, pp. BA2_01–BA2_02.

[23] T. Hirano, L. Fan, W. Lee, J. Hong, W. Imaino, S. Pattanaik, S. Chan, P. Webb, R. Horowitz, S. Aggarwal and D. Horsley, "High Bandwidth High Accuracy Rotary Microactuator for Magnetic Hard Disk Drive Tracking Servos," *IEEE/ASME Trans. on Mech.*, Vol. 3, No. 3, pp.156–165, September 1998.

[24] R. Horowitz and Y. Li, "Active Suspension Vibration Vontrol with Dual-Stage Actuators in Hard-Disk Drives," *Proc. American Control Conference 2001*, Vol. 4, pp. 2786–2791.

[25] X. P. Hu, "Dual-Stage Control Design and Implementation Issues," *Internal Report*, Data Storage Institute, Singapore, 2002.

[26] F. Y. Huang, W. Imaino, F. Lee and T. Semba, "Active Damping in HDD actuator," *IEEE Trans. Magn.*, Vol. 37,Np. 2, pp. 847–849, March 2001.

[27] S. Imai, K. Mori and T. Okazaki, "Flutter Reduction by Centrifugal Air-Flow for High Rotation-Speed Disks," *Proc. Int. Conf. Micromechanics for Information and Precision Equipment*, Tokyo, Japan, July 20–23, 1997.

[28] IBM Company Website [Online], *http://www.ibm.com*, March 2001.

[29] IBM Company Website [Online], Limits of Magnetic Recording, *http://www.almaden.ibm.com/st/projects/limits*, May 2002.

[30] M. Karaman and W. C. Messner, "Robust Dual-Stage HDD Track Follow Control Systems Design for Hand Off Shaping," *Digest of Asia-Pacific Magnetic Recording Conference 2002*, pp. BA5-01–BA5-02.

[31] M. Kobayashi, S. Nakagawa, T. Atsumi and T. Yamaguchi, "High Bandwidth Servo Control Designs for Magnetic Disk Drives," *Proc. IEEE / ASME Inter-*

national Conference on Advanced Intelligent Mechatronics 2001, Vol. 2, pp. 1124–1129.

[32] M. Kobayashi, S. Nakagawa and S. Nakamura, "A Phase-Stabilized Servo Controller for Dual-Stage Actuators in Hard-Disk Drives," *Digest of Asia-Pacific Magnetic Recording Conference 2002*, pp. BA4-01–BA4-02.

[33] S. Koganezawa, T. Hara, Y. Uematsu and T. Yamada, "Effect of Dual-Stage Actuator on Positioning Accuracy in 10k rpm Magnetic Disk Drives," *IEEE Trans. on Magn.*, Vol. 37, No. 2, pp. 955–958, March 2001.

[34] S. Koganezawa, K. Takashi, Y. Uematsu, T. Yamada, S. Hasegawa and T. Ueno, "A Flexural Piggyback Milli-Actuator for Over 5GBit/in^2 density Magnetic Recording," *IEEE Trans. on Magn.*, Vol. 32, No. 5, pp. 3908–3910, September 1996.

[35] Z. M. Li, G. Guo, B. M. Chen and T. H. Lee, "Optimal Track-Following Design for the Highest Tracks per Inch in Hard-Disk Drives," *J. Info. Storage Proc. Syst.*, 3(1/2), pp. 27–41, January/April 2001.

[36] L. Ljung, *System Identification : Theory for the User*, Prentice Hall, 2nd edition, 1999.

[37] Y. Lou, P. Gao, B. Qin, G. Guo, E. H. Ong, A. Takada and K. Okada, "Dual-Stage Servo with On-Slider PZT Microactuator for Hard-Disk Drives," *IEEE Trans. Magn.*, Vol. 38. No. 5, pp. 2183–2185, September 2002.

[38] Maxtor Company Website [Online], PC Storage Solutions, *http://www.maxtor.com/en/solutions/enterprise/desktop_computing-/pc_storage/index.htm*, January 2003.

[39] J. S. McAllister, “Characterization of Disk Vibrations on Aluminium and Alternate Substrates,” *IEEE Trans. on Magn.*, Vol. 33, No. 1, pp. 968–973, January 1997.

[40] J. S. McAllister, “The Effect of Disk Platter Resonances on Track Misregistration in 3.5” Disk Drives,” *IEEE Trans. on Magn.*, Vol. 32, No. 3, pp. 1762–1766, May 1996.

[41] W. Messner and R. Ehrlich, “A Tutorial on Controls for Disk Drives,” *Proc. of American Control Conference*, pp. 408–420, Arlington, VA June 25-27, 2001.

[42] C. Mohtadi, “Bode’s Integral Theorem for Discrete-Time Systems,” *IEE Proc.*, Vol. 137, Pt. D., No. 2, pp. 57–66, March 1990.

[43] I. Naniwa, S. Nakamura, S. Saegusa and K. Seto, “Low Voltage Driven Piggy-Back Actuator of Hard Disk Drives,” *Proc. 12th IEEE Int. Conf. MEMS*, pp. 49–52, 1999.

[44] C. K. Pang, E. H. Ong and G. Guo, “Experimental Dynamic Modeling and Characterisations of Disk Platter Resonances,” *Digest of Technical Papers IEEE International*, pp. BS–12, Magnetics Conference, INTERMAG Europe 2002.

[45] Polytec Website [Online], *http://polytec.de*

[46] I. Y. Shen, “Closed-Form Forced Response of a Damped, Rotating, Multiple Disks/Spindle System,” *Journal of Applied Mechanics*, Vol. 64, June 1997.

[47] I. Y. Shen and C.-P. R. Ku, “Nonclassical Vibration Analysis of a Multiple Rotating Disk and Spindle Assembly,” *Journal of Applied Mechanics*, Vol. 64, March 1997.

[48] A. B. Stanbridge and D. J. Ewins, “Modal Testing Using a Scanning Laser Doppler Vibrometer,” *Mech. Sys. and Signal Processing*, 1999.

[49] A. B. Stanbridge, M. Martarelli and D. J. Ewins, “Measuring Area Mode Shapes with a Scanning Laser Doppler Vibrometer ,” *IMAC XVII*, 1999.

[50] S.-M. Suh, C. C. Chung, “Active Resonance Control for High Speed and High TPI in Hard-Disk Drives,” *12th Annual Sympnosium on Info. Storage and Processing Systems*, June, 2001.

[51] S.-M. Suh, C. C. Chung and S.-H. Lee, “Servo Controller Design for High Bandwidth HDDs,” *Digest of Technical Papers IEEE International*, BS–01, Magnetics Conference, INTERMAG Europe 2002.

[52] Y. Soeno, S. Ichikawa, T. Tsuna, Y. Sato and I. Sato, “Piezoeletric Piggy-Back Microactuator for Hard Disk Drive,” *IEEE Trans. on Magn.*, Vol. 35, No. 2.

[53] M. Tokuyama, *et al.*, “Development of a Φ-Shaped Actuated Suspension for 100 kTPI Hard-Disk Drives,” *IEEE Trans. Magn.*, Vol. 37, No. 4, pp. 1884–1886, 2001.

[54] H. Toshiyoshi, “Microactuators for Hard Disk Drive Head Positioning” [Online], *http://toshi.fujita3.iis.u–tokyo.ac.jp/research_project/PDF%20papers/IIS-symp2002-HT.pdf*

[55] P. Weaver and R. Ehrlich, “The Use of Multirate Notch Filters in Embedded-Servo Disk Drives,” *Proc. American Control Conference*, pp. 4156–4160, June 1995.

[56] W. E. Wong, G. Guo, A. Al Mamum, W. Ye and J. Zhang, "A Position Encoding and Decoding Scheme for Ultra High Density Magnetic Recording," *Digest of Asia-Pacific Magnetic Recording Conference 2002*, pp. WE-P-08-01–WE-P-08-02.

[57] D. Wu, "Study on High Performance Dual-Stage Servomechanism in Hard-Disk Drives," *PhD Thesis*, National University of Singapore, 2002.

[58] D. Wu, G. Guo and T. C. Chong, "Analysis and Comparison of Resonance Compensation in Dual-Stage Actuation System of HDDs," *Proc. of American Control Conference 2001*, pp. 3824–3829, Vol. 5, pp. 3824–3829.

[59] D. Wu, G. Guo and T. C. Chong, "Mid-Frequency Disturbance Supression via Micro-Actuator in Dual-Stage HDDs," *IEEE Trans. on Magn.*, Vol. 38, No. 5, September 2002.

[60] B. Wu and E. Jonckheere, "A Simplified Approach to Bode's Theorem for Continuous-Time and Discrete-Time Systems," *IEEE Trans. Automatic Control*, Vol. 36, No. 11, pp. 1797–1802, November 1992.

[61] T. Yamaguchi and S. Nakagawa, "Recent Control Technologies for Fast and Precise Servo System of Hard Disk Drives," *Proc. of 6th International Workshop on Advanced Motion Control*, p. 69-73, Nagoya, Japan, 2000.

[62] J. L. Zhang, S. Weerasooriya, T. Huang and T. S. Low, "Modified AFC Runout Cancellation and its Influence on Track Following," *Proc. Int. Conf. Industrial Electronics, Control and Instrumentation*, pp. 35–40, IECON 97, 1997.

[63] Z. Zhang, *et al.*, “Magnetic Recording Demonstration Over 100 Gb/in^2,” *IEEE Trans. Magn.*, Vol. 38, No. 5, pp. 1861–1866, September 2002.

Curriculum Vitae

PANG Chee Khiang received his B.Eng.(Hons) degree in electrical and computer engineering from National University *of* Singapore (NUS) in June 2001. From July 2001 to February 2003, he is pursuing a Master of Engineering degree by research in Mechatronics and Micro Systems Group of A*STAR Data Storage Institute (DSI) and is a Graduate Tutor in NUS. His current research interests include linear systems theory, advance loop shaping techniques and servo systems for future storage devices.

His research work related to this dissertation resulted in the following publications:

1. C. K. Pang, E. H. Ong, and G. Guo, "Experimental Dynamic Modeling and Characterizations of Disk Platter Resonances," *Digest of Technical Papers IEEE International*, pp. BS–12, INTERMAG Europe 2002, Amsterdam, The Netherlands.
2. C. K. Pang, D. Wu, G. Guo, T. C. Chong, and Y. Wang, "Suppressing Sensitivity Hump in HDD Dual-Stage Servo Systems," *IIP/ISPS Joint MIPE'03*, pp. MC–11, June 16–18, 2003, Yokohama, Japan.
3. C. K. Pang, D. Wu, G. Guo, T. C. Chong, and Y. Wang, "Suppressing Sensitivity Hump in HDD Dual-Stage Servo Systems," submitted to *Journal of Microsystems Technology.*